# Unveiling the Formation of Atmospheric Oxygenated Organic Molecules under Anthropogenic-Biogenic Interactions: Insights from Binned Positive Matrix Factorization on Multi-Subrange Mass Spectra

- 5 Junchao Yin<sup>1, #</sup>, Yuliang Liu<sup>1, 2, #</sup>, Wei Nie<sup>1, 2, \*</sup>, Chao Yan<sup>1, 2</sup>, Qiaozhi Zha<sup>1, 2</sup>, Yuanyuan
- 6 Li<sup>1</sup>, Dafeng Ge<sup>1</sup>, Chong Liu<sup>1, 3</sup>, Caijun Zhu<sup>1, 2</sup>, Xuguang Chi<sup>1, 2</sup>, and Aijun Ding<sup>1, 2</sup>
- 7 <sup>1</sup> Joint International Research Laboratory of Atmospheric and Earth System Research,
- 8 School of Atmospheric Sciences, Nanjing University, Nanjing, 210023, China
- 9 <sup>2</sup> National Observation and Research Station for Atmospheric Processes and
- 10 Environmental Change in Yangtze River Delta, Nanjing, 210023, China
- Now at Hubei Province Academy of Eco-Environmental Sciences, Wuhan, China
- \* Corresponding author: niewei@nju.edu.cn
- 13 # These authors contributed equally to this work

14

15

16

17

18

19 20

21

22

23

2425

26

27

28 29

30

31

32

33

3435

36

1

2

3 4

# **Abstract**

Oxygenated organic molecules (OOMs), which are low-volatility intermediates produced via volatile organic compound (VOC) oxidation, play a critical role in secondary organic aerosol (SOA) formation through gas-to-particle conversion. Despite recent advancements in OOM characterization, the high complexity of OOM spectra poses a significant challenge in the interpretation of their sources. This study investigates OOM formation in a Chinese megacity using an improved analytical strategy that integrates binned Positive Matrix Factorization on multiple sub-range mass spectral analysis. Unlike traditional approaches that handle mass spectral peak identification and chemical interpretation sequentially, our method simultaneously optimizes both, reducing uncertainties associated with peak assignment and chemical analysis. The method successfully identified 2571 OOM molecules and systematically revealed major OOM formation pathways through 11 distinct factors: five daytime photochemical processes, four nighttime NO<sub>3</sub>-driven oxidation processes, and two regional mixed sources. Notably, this approach enabled the successful separation of sesquiterpene oxidation products in ambient measurements—compounds previously unidentified by traditional full-mass-range analysis due to their weak signals. The method captured dynamic changes in OOM composition under varying environmental conditions, demonstrating the influence of temperature and NO<sub>x</sub> levels on OOM formation, as well as the volatility-dependent patterns influenced by condensation sink. This improved analytical strategy provides new insights into atmospheric OOM chemistry and establishes a robust foundation for future studies of VOCs-OOMs-SOA

# 1 Introduction

Secondary organic aerosol (SOA) constitutes a major component of submicron aerosols in the global troposphere (Zhang et al., 2007; Jimenez et al., 2009), significantly impacting climate (IPCC, 2023) and human health (Lim et al., 2012; Shiraiwa et al., 2017). Understanding the sources and formation mechanisms of SOA is therefore crucial for developing effective strategies for air pollution mitigation.

Volatile organic compounds (VOCs) are widely recognized as the principal precursors of SOA (Hallquist et al., 2009; Ziemann and Atkinson, 2012). To a large extent, the transformation of VOCs into SOA proceeds through oxygenated organic molecules (OOMs) as key intermediates (Ehn et al., 2014; Nie et al., 2022). This process begins with the oxidation of VOCs, producing organic peroxy radicals (RO<sub>2</sub>), which then undergo diverse reaction pathways to form OOMs. The reactions of RO<sub>2</sub>, governed by unimolecular processes or bimolecular interactions with atmospheric species such as nitrogen oxides (NO<sub>x</sub>), hydroperoxyl radicals (HO<sub>2</sub>), and other RO<sub>2</sub> radicals (Orlando and Tyndall, 2012; Goldman et al., 2021), play a pivotal role in the functionalization of organic molecules. In addition, recent advances in chemical ionization mass spectrometry have enabled the detection of previously unobserved highly oxygenated products (Junninen et al., 2010; Jokinen et al., 2012; Lee et al., 2014), highlighting efficient functionalization pathways through RO2 autoxidation and dimerization (Ehn et al., 2014; Bianchi et al., 2019). Along with the functionalization, organic species tend to increase their oxygen content and reduce their volatility, thus facilitating aerosol formation (Riccobono et al., 2014; Tröstl et al., 2016; Mohr et al., 2019).

Recent studies have made substantial progress in understanding the formation of OOMs from common atmospheric precursors such as terpenes, isoprene, aromatics, and alkanes. Pioneer laboratory studies have provided key parameters of OOM formation from these VOC precursors, including the yield and characteristic profile of OOM under distinct and relatively simple chemical settings (Jokinen et al., 2015; Richters et al., 2016; Molteni et al., 2018; Zhao et al., 2021; Wang et al., 2021). However, it is difficult to interpret ambient OOM formation based on laboratory studies. There are two critical challenges. First, ambient atmosphere represents a complex interplay of multi-precursor, where interactions during oxidation processes—such as oxidant competition and RO<sub>2</sub> cross-reactions—give rise to significant non-linear effects (McFiggans et al., 2019; Heinritzi et al., 2020; Takeuchi et al., 2022; Nie et al., 2023). This means, even if VOC precursors can be well measured in an ambient environment, OOM formation cannot be explained by a direct summation of individual precursor systems informed by laboratory studies. Second, laboratory simulation conditions may

also deviate from real atmospheric conditions, particularly the oxidation processes and RO<sub>2</sub> chemistry could be distorted by the unrealistically high oxidant concentrations (Peng and Jimenez, 2020; Kenagy et al., 2024).

Currently, understanding OOM formation in the atmosphere primarily relies on analyses of ambient data. In the real atmosphere with complex precursors and oxidants, thousands of OOMs have been identified (Nie et al., 2022; Guo et al., 2022b; Zheng et al., 2023; Tian et al., 2023; Yuan et al., 2024; Liu et al., 2021, 2023, 2024). The vast volume and high complexity of mass spectral data pose significant analytical challenges. To tackle this, Positive Matrix Factorization (PMF) (Ulbrich et al., 2009; Zhang et al., 2011) has been applied to extract key processes in OOM formation (Yan et al., 2016; Massoli et al., 2018; Ge et al., 2024; Liu et al., 2021, 2023, 2024). In PMF application, two critical aspects demand attention. First, PMF-resolved factors represent processes governed by source-sink dynamics. While maximizing the mass range (i.e., number of OOM molecules) input to PMF increases the scope of information, this approach may misattribute OOMs from the same sources to distinct factors due to volatility-dependent condensation losses (Peräkylä et al., 2020), thereby undermining the source attribution capability of PMF. To address this, an approach that divides mass spectra into smaller subranges for separate PMF analysis has been proposed, which minimizes sink-induced variations and enables better source process resolution (Zhang et al., 2020). Second, accurate PMF results depend on the quality of the input data. In field observations, OOM mass spectra contain overlapping peaks, and lower resolution instruments often fail to determine accurate molecular formulas. High-resolution (HR) data, when processed using direct peak-fitting methods, can introduce biases due to limited prior knowledge and subjective decisions during peak assignment. A recently developed approach, known as binPMF, circumvents these issues by using m/z-segregated raw spectral data as the input, which preserves HR information without relying on potentially inaccurate peak fitting (Zhang et al., 2019).

In this study, we employ an improved mass spectral analysis strategy that combines binPMF with multiple sub-range spectral analysis to address analytical challenges in OOM source retrival. We investigate OOMs measured by a nitrate-based Chemical Ionization-Atmospheric Pressure interface-Time of Flight mass spectrometer (CI-APi-TOF) during spring in Nanjing, a megacity in Eastern China characterized by a mix of intense anthropogenic emissions (Ding et al., 2013, 2016) and biogenic contributions (Liu et al., 2021; Xu et al., 2021). This complex environment, characterized by multiprecursor interactions and varying oxidation conditions, provides an ideal context to test and refine our analytical approach. We apply binPMF analysis on three m/z ranges to identify main OOM formation pathways. We also examine the response of OOM compositions and properties to multiple environmental conditions.

76

77

78

79

80

81

82

83

84

85

86

87

88

89 90

91

92

93

94 95

96

97

98

99

100

101102

103

104

105

106107

108

109

110

111

112

# 2 Methodology

#### 2.1 Study site

All measurements in this study took place between April 19 and May 25, 2019, at the Station for Observing Regional Processes of the Earth System (SORPES), situated on Nanjing University's Xianlin campus within China's Yangtze River Delta region. This station is exposed to diverse atmospheric influences, including fossil fuel combustion, biomass burning, dust processes and biogenic emissions. Detailed information of the SORPES station has been comprehensively documented in multiple previous researches (Ding et al., 2013; Nie et al., 2015; Ding et al., 2016; Wang et al., 2018; Liu et al., 2019).

#### 2.2 Instrumentation

A chemical ionization atmospheric pressure interface time-of-flight mass spectrometer with nitrate reagent ions (nitrate CI-APi-TOF; Aerodyne Research Inc. and Tofwerk AG) was used to detect sulfuric acid (SA) and OOMs in ambient atmosphere. The working principles (Jokinen et al., 2012; Lee et al., 2014) and sampling settings (Liu et al., 2021, 2023) of the instrument have been given in previous literatures. The concentrations of OOMs were quantified using an empirical method based on the ionization and transmission efficiency of the CI-APi-TOF (Eq. 1) (Heinritzi et al., 2016).

136 
$$[OOM_i] = ln \left( 1 + \frac{\sum_{n=0}^{1} [OOM_i \cdot (HNO_3)_n \cdot NO_3^- + (OOM_i - H)^-]}{\sum_{n=0}^{2} [(HNO_3)_n \cdot NO_3^-]} \right) \times C \times T_i$$
 (1)

Here [OOM<sub>i</sub>] is the concentration (molecules cm<sup>-3</sup>) of an individual OOM. On the right side of the equation, the numerator in the parentheses is the detected total signals (ions s<sup>-1</sup>) of one OOM charged by nitrate ions in adduct-forming and deprotonated ways, and the denominator is the sum of all reagent ions signals (ions s<sup>-1</sup>). *C* is an H<sub>2</sub>SO<sub>4</sub> based calibration factor, with a value of 5.1×10<sup>9</sup> molecules cm<sup>-3</sup> in this study, obtained from a calibration using H<sub>2</sub>SO<sub>4</sub> following the method of previous study (Kürten et al., 2012) and a consideration of diffusion loss in the sampling tube by assuming that all OOMs detected have the same ionization efficiency as H<sub>2</sub>SO<sub>4</sub>. This assumption is generally valid for highly oxygenated molecules (typically with more than 6 oxygen atoms) due to their efficient clustering with NO<sub>3</sub><sup>-</sup> (Hyttinen et al., 2015; Riva et al., 2019)(Ehn et al., 2014; Hyttinen et al., 2015). However, for less oxygenated compounds—particularly those with fewer than six oxygen atoms—ionization

efficiency can be substantially lower, resulting in an underestimation of their true concentrations. Although some uncertainty remains in quantifying moderately oxidized species, the assumption remains the most practical and widely used approach for semi-quantitative analysis in related studies.  $T_i$  is a mass-dependent transmission efficiency of the APi-TOF inferred by depleting reagent ions with several perfluorinated acids (Heinritzi et al., 2016).

composition analysis employed The atmospheric multiple advanced instrumentation for comprehensive pollutant characterization. VOCs were quantified using a proton transfer reaction time-of-flight mass spectrometer (TOF 1000 ultra, Ionicon Analytik, Austria). Fine particulate matter concentrations were acquired through an integrated measurement approach combining light scattering photometry and beta radiation attenuation (SHARP Monitor 5030, Thermo Fisher Scientific). For particulate matter speciation, real-time chemical analysis was conducted with a time-of-flight aerosol chemical speciation monitor (TOF-ACSM, Aerodyne Research). Gaseous pollutants were monitored using state-of-the-art detection methods: nitrogen oxides (NO<sub>x</sub>) were analyzed using a chemiluminescence analyzer with a blue-light converter (Model 42i-TL, TEI), while ozone, sulfur dioxide, and carbon monoxide concentrations were determined respectively by ultraviolet photometry, pulsed-UV fluorescence, and infrared photometry techniques (Models 49i, 43C, and 48C, TEI). Weekly calibration was performed for all gas-phase measurements. Complementary meteorological parameters, specifically atmospheric relative humidity (RH) and air temperature, were continuously logged using an automatic weather station (AG1000, Campbell Scientific). More details about the instruments can be found in the Supplementary Information, including the flow settings of each instrument and the results of the sulfuric acid calibration and transmission efficiency characterization of the CI-APi-TOF (Fig. S1).

175

176

177

178179

180

181

182

183 184

185

186

187

188

150

151

152

153

154155

156

157

158

159

160

161162

163164

165

166

167

168169

170171

172

173

174

#### 2.3 binPMF analysis on multiple mass spectral sub-ranges

We employed Positive Matrix Factorization (PMF) on binned mass spectra (binPMF) as our primary analytical strategy to deconvolve the complex mass spectral data into interpretable source components. This method averages raw spectral data along the m/z dimension without requiring prior knowledge of chemical compositions, significantly reducing data processing complexity while maintaining analytical robustness. Specifically, after mass calibration, the raw spectra were divided into narrow bins of 0.004 Th width, and the corresponding data and error matrices were prepared following the methodology described in Zhang et al. (2019).

To address the challenges of the volatility-dependent loss variations and the orders-of-magnitude variations in signal intensity across the mass spectrum, we implemented binPMF analysis on three overlapping mass ranges: Range 1 (150-300 Th), Range 2 (250-400 Th), and Range 3 (350-500 Th). Such mass range division can generally

separate heavier, more condensable OOM from lighter, less condensable ones. Therefore, this sub-range strategy minimizes the impact of sink-induced variations while enabling better resolution of source processes. The overlapping regions between adjacent ranges (250-300 Th and 350-400 Th) serve as crucial links for cross-validating and comparing factors across different mass ranges. The relative changes in the source factor profiles between the different sub-ranges contribute to the dynamic nature of the combined factor spectra. Specifically, variations in the mass spectral features across the sub-ranges lead to distinct temporal and compositional changes in the final factor profiles. This dynamic analysis approach enables better resolution of source processes and provides a more robust representation of the underlying sources. By minimizing sink-induced variations and leveraging the temporal and compositional overlap between the ranges, we achieve improved factor separation and identification.

The PMF analysis was performed using Source Finder (SOFI), an Igor Pro-based interface for efficient source apportionment analysis. After determining the optimal solution for each mass range, high-resolution peak fitting was conducted through tofTools (version 6.11) in MATLAB (MathWorks Inc.) to obtain detailed molecular composition of OOMs in each resolved factor.

206

207

208

209210

211

212

213

214

215216

217218

219

220221

222223

224

225

226

189

190 191

192

193 194

195

196

197

198

199

200

201

202203

204

205

#### 3 Results

### 3.1 Overview

The average binned mass spectrum of detected ions (m/z 150-500) is shown in Figure 1a. Notably, mass spectral signals at m/z 201, which were dominated by intense nitrophenol peaks (C<sub>6</sub>H<sub>5</sub>OHNO<sub>3</sub>C<sub>6</sub>H<sub>5</sub>NO<sub>3</sub>NO<sub>3</sub><sup>-</sup>), were excluded to prevent their disproportionate influence on the PMF results. The mass spectrum was divided into three ranges: R1 (150-300 Th), R2 (250-400 Th), and R3 (350-500 Th), with binPMF analysis performed independently on each range to determine optimal solutions. This approach enabled successful decomposition of complex mass spectra into distinct factors, effectively separating overlapping peaks. Details regarding factor selection criteria and diagnostic evaluations of PMF solutions for each range are provided in the Supplementary Information. The factor-specific spectra obtained from binPMF exhibited systematic chemical patterns, facilitating high-resolution peak fitting. Compared to traditional HR fitting of raw spectra, this binPMF-based approach improved molecular formula assignments through purified factor spectra and systematic pattern recognition. Through peak fitting and reconstruction of binPMF factor spectra, we identified 2571 OOM molecules in the mass range of m/z 150-500 Th, comprising CHO and CHON compounds. Nitrated phenols were excluded from this analysis given their relatively well-characterized formation pathways. The mass defect (MD) plot (Fig. 1b), colored by effective oxygen number (total oxygen minus two oxygen atoms from nitrate groups), shows characteristic chemical gradient or clustered distribution. The majority of observed OOMs include 3–6 effective oxygen atoms, accounting for 85% of the total signals. This high oxygenation distinguishes these compounds from traditional oxygenated VOCs (typically 1-2 oxygen atoms). The prevalence of these highly oxygenated species indicates extensive atmospheric oxidation processes, which will be discussed subsequently.

227

228

229

230

231232

233234

235

236237

238 239

240241

242

243

244

245

246247

248

249

250

251 252

253

254

255

256

257258

259

260

261

262

263

264

265

266267

Beyond peak identification, binPMF analysis provided insights into the atmospheric evolution of OOMs. An integrated comparison of binPMF results across the three spectral subranges was performed to identify common factors. Factors with strong correlations (r > 0.70) in both spectral profiles and time series across overlapping subranges were classified as representing the same source and were merged accordingly (Figures 2 and \$2\$3-\$4\$5). Correlation analyses focused on adjacent subranges with 50 Th overlapping regions (Figure 3). While most factors demonstrated strong consistency across overlapping subranges, a few deviations were observed. For instance, the D1-AVOC-I factor exhibited a lower spectral profile correlation between R2 and R3 (r = 0.52) but was reliably identified as the same factor based on consistent temporal patterns.

In total, 11 merged factors were identified, excluding those dominated by nitrated phenols.17 merged factors are identified. These include five factors associated with daytime chemistry (denoted by the "D-" prefix), four factors linked to nighttime chemistry ("N-" prefix), and two factors with no significant diurnal patterns and six factors excluded from the following discussion. Of these six disregarded factors, five factors are dominated by nitrophenol-related compounds, and one is characterized by fluorinated contaminants. The nitrophenol (NP) factors are not further analyzed in this study, as they have been extensively investigated in previous work (Cheng et al., 2021; Song et al., 2021; Chen et al., 2022)(Cheng et al., 2021; Song et al., 2021; Chen et al., 2022). At this site, earlier binPMF analyses successfully separated NP factors (Liu et al., 2021, 2023)(Liu et al., 2021, 2023), revealing their distinct chemical signatures compared to other OOMs. Due to these clear distinctions, NP-related components are typically resolved into separate factors with minimal overlap. Therefore, their exclusion in the current analysis is not expected to affect the overall factor resolution or interpretation. The contamination factor is primarily composed of various fluorinated compounds, mainly perfluorinated organic acids, which originated from the Teflon tubing used in our sampling system. The identified factors display distinct molecular compositions and volatility distributions (Figures 4 and 5). This multi-subrange PMF approach, by focusing on narrower mass windows, enhanced sensitivity to minor spectral features that full-range analyses often overlook. For example, a factor dominated by sesquiterpene oxidation products was successfully isolated using this approach; this factor would otherwise have been merged into major nighttime factors in traditional full-range PMF analysis. To the best of our knowledge, few PMF studies identified the sesquiterpene oxidation-related factor in a polluted megacity region. A detailed characterization of all the factors, including their molecular signatures, oxidation pathways, and environmental implications, is provided in subsequent sections.

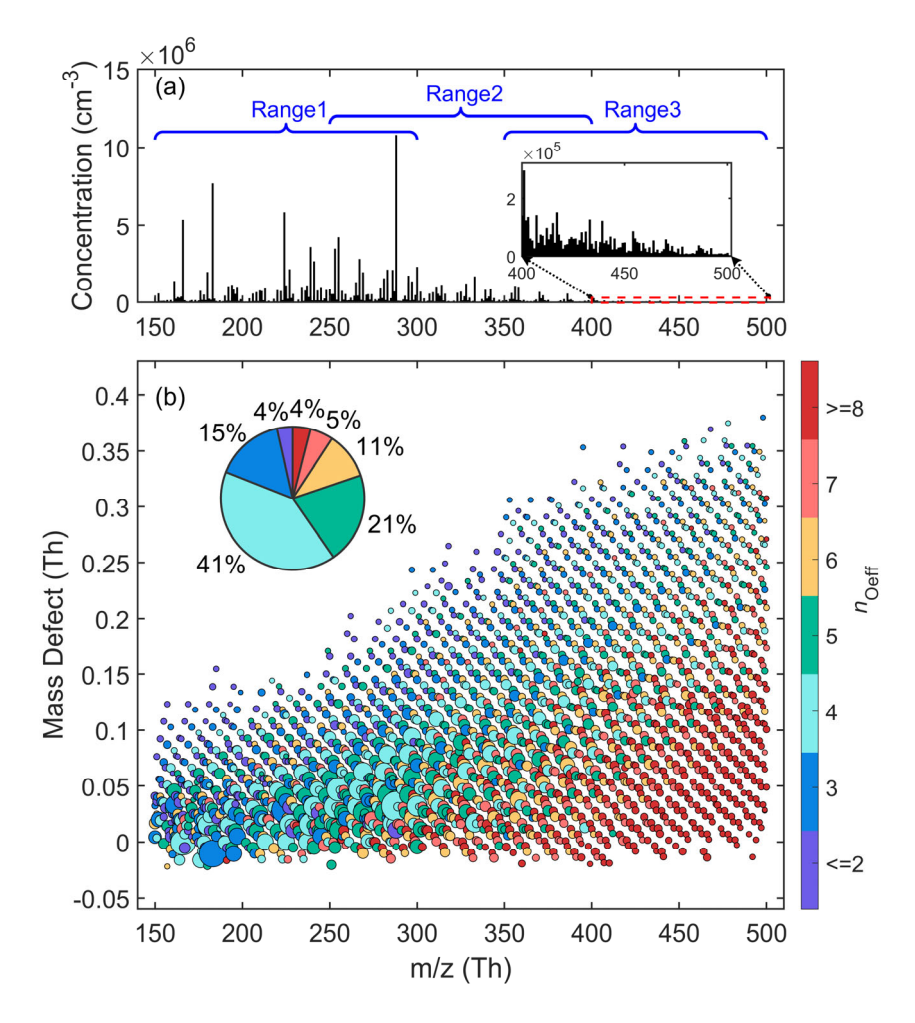
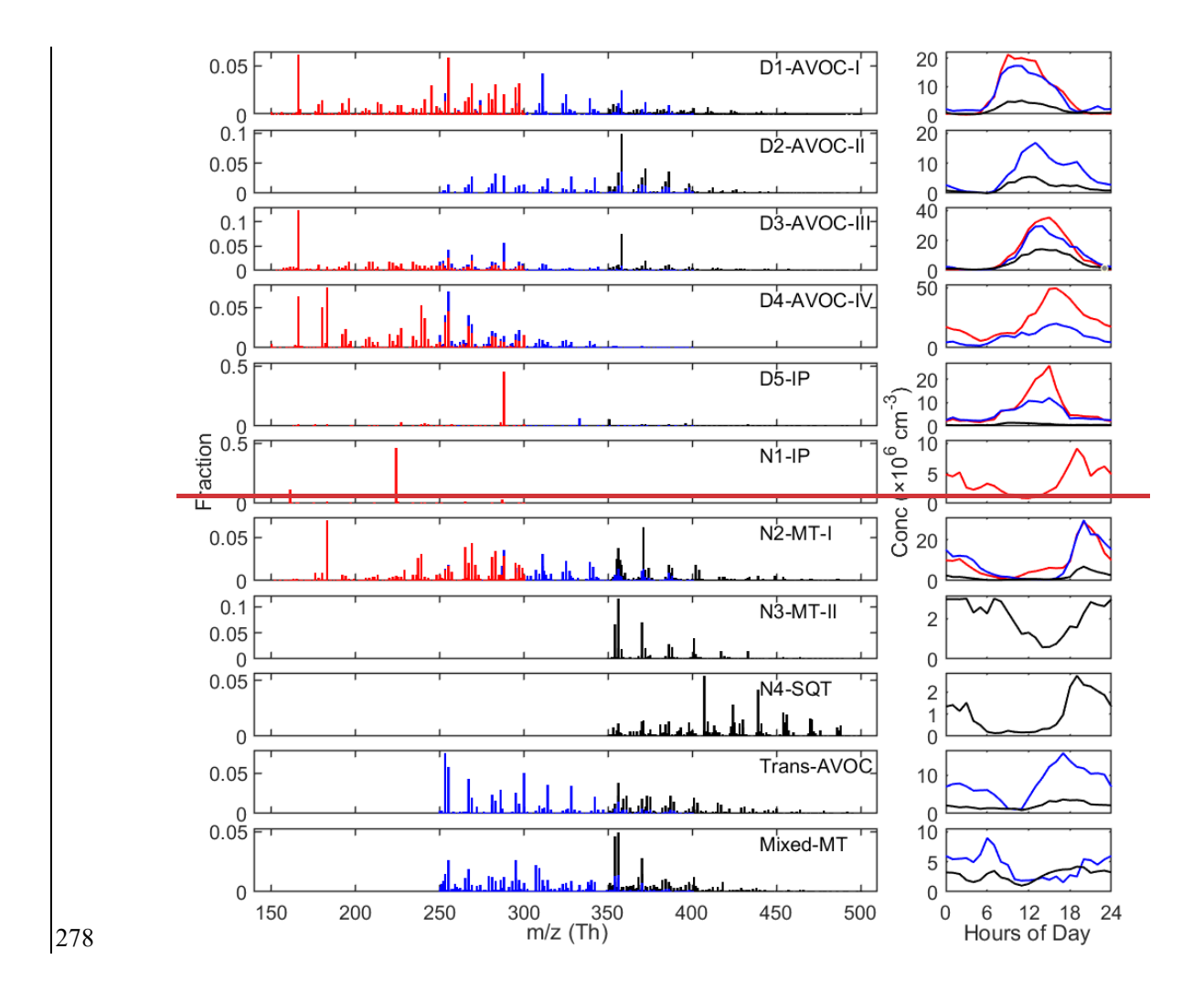


Figure 1. Overview of all non-nitro OOMs identified. (a) Combined overall mass spectrum of the three subranges. (b) Mass defect plot of OOMs identified from the reconstructed dataset based on binPMF results. Dots are colored by the number of effective oxygen atoms and scaled according to the square root of concentration. The pie chart displays the distribution of OOM fractions grouped by the number of effective oxygen atoms.



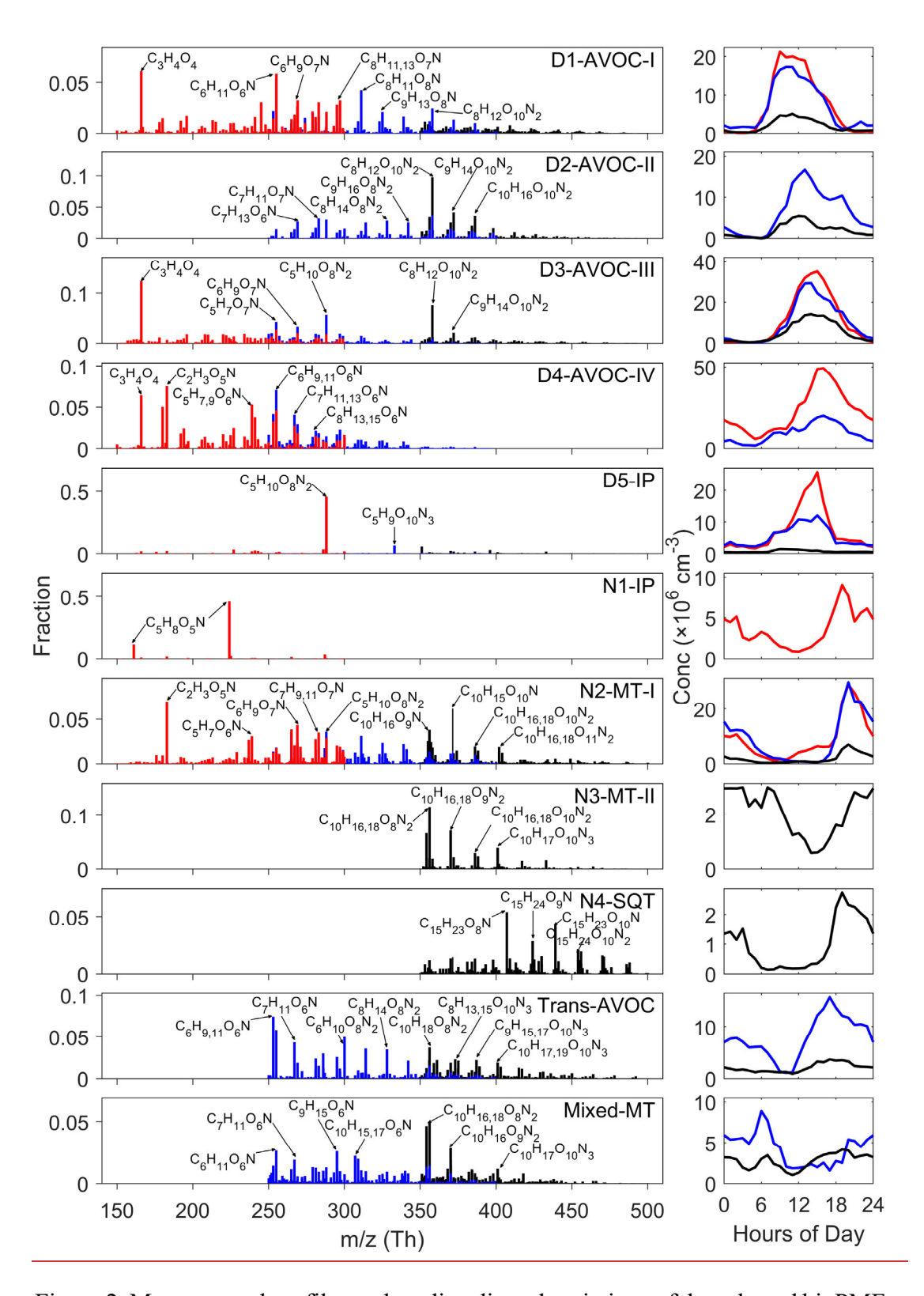


Figure 2. Mass spectral profiles and median diurnal variations of the selected binPMF factors, and the elemental formulas of major peaks are labeled above them. Factors describing the similar process were assembled, red for Range 1, blue for Range 2 and black for Range 3.

Table 1 Summary of molecular characteristics of eleven discussed factors.

Factors	Ranges	Total Conc. (cm <sup>-3</sup> )	DBE OSc	O:C	N:C	Peak time	Fingerprint molecules
D1-AVOC-I	1,2,3	1.74E+07	2.78 -0.19	0.88	0.11	9:00-13:00	C <sub>x</sub> H <sub>2x-1</sub> O <sub>6</sub> N, C <sub>x</sub> H <sub>2x-5</sub> O <sub>8</sub> N, C <sub>x</sub> H <sub>2x-4</sub> O <sub>10</sub> N <sub>2</sub>
D2-AVOC-II	2,3	1.11E+07	1.81 -0.73	0.89	0.17	13:00; 19:00	$C_xH_{2x-2}O_8N2$ , $C_xH_{2x-4}O_{10}N_2$
D3-AVOC-III	1,2,3	3.25E+07	2.73 0.13	1.01	0.10	13:00-15:00	$C_xH_{2x-4,2x-6}O_5$ , $C_xH_{2x-3}O_7N$ , $C_xH_{2x-5}O_{7,8}N$
D4-AVOC-IV	1,2	2.92E+07	2.16 -0.12	1.02	0.13	15:00-16:00	$C_xH_{2x-2}O_4$ , $C_xH_{2x-1,2x-3}O_6N$
D5-IP	1,2,3	2.53E+07	1.55 -0.39	1.31	0.28	15:00	$C_5H_{10}O_8N_2$ , $C_5H_9O_{10}N_3$
N1-IP	1	1.17E+07	1.99 -0.35	0.94	0.14	19:00	$C_5H_8O_5N\cdot$
N2-MT-I	1,2,3	1.84E+07	2.35 -0.21	1.03	0.16	19:00-20:00	$C_xH_{2x-3}O_{6,7}N,C_{10}H_{15,17}O_xN,C_{10}H_{16}O_xN_2$
N3-MT-II	3	2.67E+06	1.75 -0.79	0.95	0.21	0:00-3:00	$C_{10}H_{16,18}O_xN_2$ , $C_{10}H_{17}O_xN_3$
N4-SQT	3	2.18E+06	2.99 -0.64	0.78	0.12	19:00	$C_{15}H_{23,25}O_xN$ , $C_{15}H_{24}O_xN_2$
Trans-AVOC	2,3	1.47E+07	1.70 -0.64	1.01	0.21	/	$C_xH_{2x-1,2x-3}O_6N$ , $C_xH_{2x-2}O_8N_2$ , $C_xH_{2x-3}O_{10}N_3$
Mixed-MT	2,3	8.96E+06	2.13 -0.79	0.78	0.14	/	$C_xH_{2x1,2x3}O_6N,C_{10}H_{15,17}O_xN,C_{10}H_{16,18}O_xN_2$

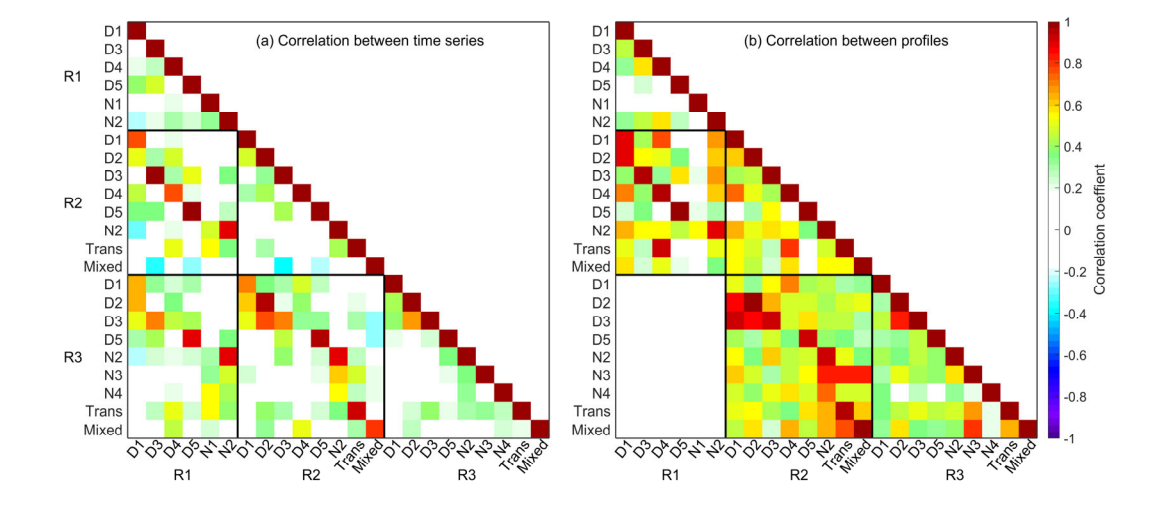


Figure 3. Correlation coefficient between (a) time series and (b) profiles of factors across all subranges. Values of correlation coefficient are shown as colors and numerically. The analysis of profile correlations is confined to the regions of overlap between the profiles.

# 3.2 Daytime chemistry

Among the identified factors, five were predominantly associated with daytime oxidation processes. Four of these factors were derived from anthropogenic VOC precursors, while one factor was attributed to the oxidation of biogenic isoprene. These daytime factors exhibited distinct temporal patterns that closely aligned with photochemical oxidation activities.

#### 3.2.1 D1-AVOC-I

301

302303

304

305 306

307

308309

310

311

312313

314

315

316317

318

319

320

321

322

323324

325

326

327

328

329330

331

332

333

334

335

336

337

338339

340

This factor exhibits a pronounced diurnal pattern characterized by low nighttime concentrations and the earliest onset of daytime increase, reaching a plateau earlier than other factors (Fig. 2). Its correlations with solar radiation and OH radical, particularly with the 'Arom × OH' proxy (representing aromatics-OH reaction rate), support its attribution to initial-stage photochemical processes (Fig. \$557). Among all daytime factors, this factor shows the highest averaged double bond equivalent (DBE) (Table 1), primarily attributed to aromatic oxidation products (DBE>2). The most abundant aromatic-derived species are  $C_xH_{2x-5}O_{6-9}N$  (x = [5, 17]), consistent with products observed in OH-initiated oxidation experiments of aromatics under NO<sub>x</sub>-influenced conditions (Tsiligiannis et al., 2019; Zaytsev et al., 2019). Notably, a similar factor, previously identified as 'Aro-OOM' in our summer and winter observations at the same site, showed comparable chemical characteristics (Liu et al., 2021, 2023). While aromatic products contribute significantly, the dominant components are C<sub>x</sub>H<sub>2x-1</sub>O<sub>6</sub>N (x = [3, 13]) series (Table \$\frac{\$4\$}{\$2}\$), likely originating from alkane oxidation. The CHO compounds are predominantly formed through the RO2+NO pathway, followed by alkoxy radical (RO) termination or fragmentation. The temporal behavior, oxidant dependency, and molecular compositions collectively characterize this factor as firstgeneration oxidation products of mixed anthropogenic VOCs.

#### **3.2.2 D2-AVOC-II**

As the only daytime factor lacking Range 1 components, this factor exhibits the lowest non-nitrate percentage among all daytime factors (Fig. 4). It is primarily composed of dinitrates, including  $C_xH_{2x-2}O_8N_2$  (x = [6, 18]) and  $C_xH_{2x-4}O_{10}N_2$  (x = [7, 12]), indicating that they should form through multi-generational oxidation processes. The first series also account for a substantial fraction in the Aliph-OOM factor in the summertime at this site(Liu et al., 2021) (Liu et al., 2021). These near-saturated compounds are likely oxidation products of aliphatic precursors under strong NO<sub>x</sub> influence in urban air, as proposed in previous laboratory studies (Algrim and Ziemann, 2019; Wang et al., 2021)(Algrim and Ziemann, 2019; Wang et al., 2021). Notably, it cannot be denied that C<sub>10</sub>H<sub>18</sub>O<sub>8</sub>N<sub>2</sub> may also originate from terpene oxidation (Luo et al., 2023)(Luo et al., 2023). The first series represents typical aliphatic products, while Tthe latter corresponds to second-generation aromatic products observed in laboratory studies (Tsiligiannis et al., 2019; Wang et al., 2020)(Tsiligiannis et al., 2019; Wang et al., 2020). The temporal profile of this factor shows both a delayed onset and a peak concentration lagging the D1-AVOC-I factor, with maximum levels occurring around 13:00 LT. This timing is consistent with the behavior of multi-generational oxidation products. Notably, this factor shows a secondary peak around 19:00 LT (Fig. 2), likely attributed to NO<sub>3</sub> oxidation. It is important to note that NO<sub>3</sub> primarily reacts with carbon-carbon double bonds, targeting not only alkenes but also the unsaturated structures formed from OH-initiated aromatic ring opening during daytime. Therefore, we propose this factor represents a mixed oxidation process where precursors undergo initial OH oxidation with NO<sub>x</sub> termination during the day, followed by further NO<sub>3</sub> oxidation at night. This mechanism explains the high organic nitrate fraction (93%) observed in this factor.

#### **3.2.3 D3-AVOC-III**

341

342

343344

345

346

347

348

349350

351

352353

354355

356

357

358

359

360

361362

363

364

365

366367

368

369370

371

372

373 374

375

376

377

378

379

380

This factor shows strong correlations with O<sub>3</sub> and temperature (Fig. \$5\$57). It contains the highest proportion of CHO compounds, with characteristic molecules  $C_xH_{2x-4}O_5$  (x = [4, 10]) and  $C_xH_{2x-6}O_5$  (x = [5, 10], Table \$\frac{\$4\frac{84}}{2}\$). These compounds are typical aromatic oxidation products While their high DBE values and relatively high contributions from C<sub>6</sub>-C<sub>8</sub> species suggest a strong influence from aromatic oxidation, we acknowledge that contributions from isoprene and monoterpene oxidation under low-NO<sub>x</sub> conditions cannot be ruled out. Similar factors were identified in previous studies, including an "isoprene afternoon" factor at a forest site in Alabama(Massoli et al., 2018) (Massoli et al., 2018), a "Daytime type-3" factor at a rural site in Finland (Yan et al., 2016), and a "Temp-related" factor in an urban environment (Liu et al., 2021), all showing temperature dependence and potential biogenic influence. While correlating with O<sub>3</sub>, it is important to note that O<sub>3</sub> itself does not oxidize aromatics. Instead, OH radical serves as the primary oxidant for aromatics, alkanes, and alkenes during daytime. The factor peaks in the afternoon, during periods of high temperatures and low NO concentrations. These conditions favor RO<sub>2</sub> termination by HO<sub>2</sub> (also at its peak), leading to CHO compound formation (Newland et al., 2021; Zheng et al., 2023). Elevated temperatures suppress the RO<sub>2</sub> + NO reaction toward nitrate formation, instead promoting alkoxy RO and NO<sub>2</sub> production (Perring et al., 2013). This RO termination involves fragmentation reactions, explaining the abundance of C<sub>3</sub>-C<sub>4</sub> fragmentation products observed. The additional NO<sub>2</sub> production contributes to O<sub>3</sub> formation. Therefore, we propose this factor represents a characteristic photochemical process associated with O<sub>3</sub> formation, with anthropogenic VOCs as primary reactants dominated by anthropogenic VOCs, but with possible contributions from biogenic sources as well. A similar factor was previously identified at the same site during summer observations, defined as 'Temp-related' (Liu et al., 2021).

#### **3.2.4 D4-AVOC-IV**

The formation mechanism of this factor is not yet fully understood due to its complex temporal patterns and molecular composition. This factor is primarily composed of C<sub>5</sub>-C<sub>8</sub> OOMs (Fig. 4), with a daytime peak occurring around 16:00 LT (Fig. 2). The concentration does not drop to very low levels during the night, and in certain periods (2 May to 7 May and 9 May to 16 May), higher nighttime values are observed, suggesting some transport influence (Fig. S2 and S3). A significant proportion of the factor consists of non-nitrates, with the most prominent components being  $C_xH_{2x-2}O_4$  (x = [3, 9], where  $C_3H_4O_4$  has the highest concentration). These compounds have been observed in previous studies and are identified as dicarboxylic acids (Ehn et al., 2010;

Ye et al., 2021). Many  $C_xH_{2x-1}O_6N$  (x = [3, 12]) and  $C_xH_{2x-3}O_6N$  (x = [4, 14]) series were also present in this factor, which should mainly come from the oxidation of alkanes in this site (Liu et al., 2021, 2023). While direct laboratory evidence linking these molecular series to a common formation pathway is limited, theoretical considerations and recent chamber studies support their possible co-generation. Both C<sub>x</sub>H<sub>2x-2</sub>O<sub>4</sub> and C<sub>x</sub>H<sub>2x-1</sub>O<sub>6</sub>N can be derived from the same RO<sub>2</sub> precursor (C<sub>x</sub>H<sub>2x-1</sub>O<sub>5</sub>) through different termination pathways with NO. The former may form via RO radical intermediates (C<sub>x</sub>H<sub>2x-1</sub>O<sub>4</sub>) that undergo further oxidation to produce carbonylcontaining compounds, whereas the latter results from direct NO addition to RO2 forming RONO<sub>2</sub>. The mass difference between these products corresponds to a loss of one HNO<sub>2</sub> unit. A similar relationship applies between C<sub>x</sub>H<sub>2x-4</sub>O<sub>4</sub> (Table S5) and C<sub>x</sub>H<sub>2x-</sub> 3O<sub>6</sub>N, as well as C<sub>x</sub>H<sub>2x-2</sub>N<sub>2</sub>O<sub>8</sub> in R2. Recent laboratory experiments investigating the OH oxidation of alkanes under varying NO levels also observed concurrent production of carbonyl species and organic nitrates, supporting this mechanistic linkage (Wang et al., 2021)(Wang et al., 2021). These observations reinforce the idea that the cooccurrence of these compounds in the same factor likely reflects different chemical pathways stemming from shared precursors.

#### 3.2.5 D5-IP

This factor is dominated by C<sub>5</sub> compounds, particularly C<sub>5</sub>H<sub>10</sub>O<sub>8</sub>N<sub>2</sub> (Table S<sub>6</sub>). This compound, an isoprene oxidation product containing two hydroxyl and two nitrate groups, is likely formed through a two-step OH oxidation of isoprene followed by RO<sub>2</sub>+NO termination (Jenkin et al., 2015). Recent studies have identified this molecule as a major isoprene nitrate component in the upper troposphere over the Amazon rainforest, where it plays a crucial role in new particle formation (Zha et al., 2023; Curtius et al., 2024). In our previous summer observations at this site, isoprene oxidation processes exhibited stronger influences on OOMs, resulting in two distinct factors characterized by C<sub>5</sub>H<sub>10</sub>O<sub>8</sub>N<sub>2</sub>: one representing local formation and another indicating transport processes (Liu et al., 2021; Xu et al., 2021). Additionally, this factor contains substantial nitrogen-containing C<sub>10</sub> compounds in the R3 region, including  $C_{10}H_{16}O_xN_2$  (x = [8, 14]) and  $C_{10}H_{17}O_xN_3$  (x = [10, 14]), which are likely products of multi-generational processes involving OH oxidation of monoterpenes followed by RO<sub>2</sub>+NO termination reactions. Due to the relatively high NO concentration during the daytime at this site, it is unlikely that these C<sub>10</sub> substances originate from C<sub>5</sub> RO<sub>2</sub>+C<sub>5</sub>  $RO_2$ .

415

416

417

418 419

381

382

383

384

385386

387

388 389

390

391

392393

394

395

396 397

398

399

400

401 402

403

404

405

406

407

408 409

410

411 412

413

414

#### 3.3 Nighttime chemistry

In contrast to the complex photochemical processes during daytime, nighttime chemistry is driven by NO<sub>3</sub> radical oxidation of carbon-carbon double bonds, leading to factors with more distinct source characteristics. However, considering that ozone

concentrations remain relatively high during nighttime at this site (Fig. S8a), we cannot exclude a potential contribution from ozonolysis. The following four factors exhibit clear chemical signatures associated with biogenic volatile organic compounds (BVOCs) and their NO<sub>3</sub>-initiated oxidation pathwaysnighttime oxidation, with NO<sub>3</sub> chemistry playing a dominant role.

#### 3.3.1 N1-IP

425

426

427

428 429

430

431

432 433

434

435

436 437

438

439

440441

442443

444

445

446

447448

449

450451

452 453

454

455

456

457

458

This factor, exclusively present in the R1 region, exhibits elevated concentrations during nighttime with a peak at 19:00 LT (Fig. 2). The two most prominent peaks in the mass spectrum correspond to the same compound C<sub>5</sub>H<sub>8</sub>O<sub>5</sub>N, appearing at m/z 224 and 161, which represent its NO<sub>3</sub><sup>-</sup> adduct and deprotonated forms, respectively. This RO<sub>2</sub> radical originates from NO<sub>3</sub> initiated oxidation of isoprene. This RO<sub>2</sub> radical arises from the NO<sub>3</sub>-initiated oxidation of isoprene and represents the first RO<sub>2</sub> species formed in this reaction. It accounts for 57.4% of the total factor intensity (Table S76). A peak-fitted time series of C<sub>5</sub>H<sub>8</sub>O<sub>5</sub>N was extracted and compared to the time series of the N1-IP factor. As shown in Fig. S9, the two are highly correlated (R = 0.98), demonstrating that this compound can serve as a representative tracer for this factor. While this compound was also observed in our summer measurements at this site, it was previously incorporated into a broader factor representing NO<sub>3</sub>-oxidized BVOCs, including monoterpene oxidation products, due to the wider mass spectral range used in the binPMF analysis at that time (Liu et al., 2021). A series of similar RO<sub>2</sub> radicals have been reported in previous laboratory studies investigating isoprene NO<sub>3</sub> oxidation (Zhao et al., 2021). However, more highly oxygenated radicals (C<sub>5</sub>H<sub>8</sub>O<sub>6-11</sub>N) were not observed in the present study, likely due to the suppression of further RO<sub>2</sub> radical oxidation under high NO<sub>x</sub> conditions at this site.

#### 3.3.2 N2-MT-I

This factor exhibits pronounced nocturnal characteristics, with peak concentrations observed at 20:00 LT (Fig. 2). A distinctive feature of this factor is the presence of a series of nitrogen-containing RO<sub>2</sub> radicals (C<sub>10</sub>H<sub>16</sub>O<sub>8-11</sub>N), which serve as key markers of NO<sub>3</sub>-initiated monoterpene oxidation. The factor's composition is predominantly comprised of C<sub>6</sub>-C<sub>10</sub> OOMs (Fig. 4). In the R3 region, the major products are C<sub>10</sub> monoterpene-derived OOMs, consisting almost exclusively of organic nitrates, including C<sub>10</sub>H<sub>15,17</sub>O<sub>9-12</sub>N and C<sub>10</sub>H<sub>16,18</sub>O<sub>8-13</sub>N<sub>2</sub>. In contrast, R1 and R2 regions are dominated by monoterpene fragmentation products, such as C<sub>7</sub>H<sub>9</sub>O<sub>6-9</sub>N and C<sub>9</sub>H<sub>15</sub>O<sub>6-9</sub>N (Table S<sub>8</sub><del>7</del>). These molecular compositions align well with laboratory observations from NO<sub>3</sub> oxidation experiments of β-pinene and limonene (Shen et al., 2021; Guo et al., 2022a). A similar factor, previously labeled as 'BVOC-OOMs-II', was also identified in our summer measurements at this site (Liu et al., 2021).

#### 3.3.3 N3-MT-II

This factor, exclusively detected in the mass spectral sub-region R3, exhibits strong

nighttime signals with minima occurring during the afternoon (Fig. 2). The dominance of C<sub>10</sub> compounds indicates its primary composition of monoterpene oxidation products (Fig. 4). Unlike N2-MT-I, this factor features predominantly dinitrates and trinitrates (e.g., C<sub>10</sub>H<sub>16,18</sub>O<sub>8-13</sub>N<sub>2</sub> and C<sub>10</sub>H<sub>17</sub>O<sub>10-13</sub>N<sub>3</sub>), with nitrate-containing compounds accounting for 98% of its total composition, indicating that it primarily consists of multi-generation oxidation products. The abundance of multi-nitrates and nighttime maximum strongly indicates NO<sub>3</sub> participation in driving repeated oxidation processes at night. Notably, this factor persists after sunrise, unlike the rapid morning decline observed in N2-MT-I, matching the behavior of the 'BVOC-OOM-III' factor from our summer campaign (Liu et al., 2021). This suggests that NO<sub>3</sub>-initiated oxidation of monoterpenes at night is followed by further oxidation in the morning, potentially involving OH and O<sub>3</sub>, leading to the observed multi-nitrate species. Furthermore, some of the nighttime concentrations may arise from daytime oxidation products that undergo additional NO<sub>3</sub>-driven oxidation during the night. Overall, this factor represents multigenerational oxidation products, involving various oxidants during the transition between day and night. This pattern suggests a potential mechanism where NO3initiated nighttime monoterpene oxidation products undergo further oxidation, possibly involving OH, in the morning, yielding the observed multi-nitrate species.

#### 3.3.4 N4-SQT

459

460

461

462

463

464

465

466

467 468

469

470471

472

473

474 475

476

477

478

479 480

481

482

483

484

485

486

487

488

489 490

491

492

493

494 495

496 497

498 499

This factor is characterized by abundant C<sub>15</sub> highly oxygenated organic molecules (C<sub>15</sub>H<sub>23,25</sub>O<sub>6-13</sub>N, C<sub>15</sub>H<sub>24</sub>O<sub>8-12</sub>N<sub>2</sub>), attributed to sesquiterpene oxidation products (Table S109), with organic nitrates constituting 97% of the total products (Fig. 4). Similar to isoprene-derived N1-IP and monoterpene-derived N2-MT-I factors, NO<sub>3</sub>-derived C<sub>15</sub> RO<sub>2</sub> radicals (C<sub>15</sub>H<sub>24</sub>O<sub>7-13</sub>N) were detected, supported by the distinct diurnal pattern showing elevated nighttime concentrations and morning decrease (Fig. 2). However, some of the C<sub>15</sub>H<sub>24</sub>O<sub>x</sub>N<sub>2</sub> species, particularly those with higher oxygen content, are likely products of C<sub>5</sub>-RO<sub>2</sub> and C<sub>10</sub>-RO<sub>2</sub> dimerization reactions, given the presence of C<sub>5</sub>H<sub>8</sub>NO<sub>5</sub> and C<sub>10</sub>H<sub>16</sub>O<sub>x</sub>N radicals observed in other nighttime factors and their similar diurnal patterns. However, due to the detection of C<sub>15</sub> RO<sub>2</sub>, these C<sub>15</sub> substances are more likely to originate from sesquiterpene precursors. Nevertheless, given the high reactivity of sesquiterpenes toward ozone(Gao et al., 2022) (Gao et al., 2022), and the elevated nighttime O<sub>3</sub> concentrations observed at this site (Fig. S8a), we cannot rule out a potential contribution from ozonolysis. Due to their extended carbon skeleton (C<sub>15</sub>), sesquiterpene oxidation products demonstrate significantly lower volatility compared to monoterpene (C<sub>10</sub>) and isoprene (C<sub>5</sub>) products (Fig. 5), a property that recent laboratory and field studies have linked to their crucial role in early-stage new particle formation (Dada et al., 2023; Liu et al., 2024). In our previous summer measurements at this site, sesquiterpene signals were mixed with isoprene and monoterpene products without mass spectral sub-range analysis, often being overshadowed by stronger monoterpene signals (Liu et al., 2021). To our knowledge, this represents the first successful separation of sesquiterpene oxidation products in ambient measurements,

enabling a clearer understanding of NO<sub>3</sub>-driven sesquiterpene chemistry under real atmospheric conditions.

#### 3.4 Regional mixed sources

500

501

502

503

504

505

506

507

508

509

510

511 512

513

514

515

516

517

518

519

520

521522

523

524525

526

527

528

529

530

531532

533534

535

536

The remaining two factors show sustained concentrations throughout day and night with weak diurnal patterns, a characteristic feature of regional background.

#### 3.4.1 Trans-AVOC

This factor is characterized by a high abundance of nitrogen-containing compounds, particularly di- and tri-nitrates, with predominant homologous series of C<sub>x</sub>H<sub>2x-2</sub>O<sub>8</sub>N<sub>2</sub> (x = [4, 14]) and C<sub>x</sub>H<sub>2x-1, 2x-3</sub>O<sub>10,11</sub>N<sub>3</sub> (x = [7, 13]), indicating multiple RO<sub>2</sub>+NO<sub>x</sub> reactions. The molecular composition features both a high proportion of C<sub>6</sub>-C<sub>10</sub> OOMs (81%) and consistently low double bond equivalents (DBE < 2), strongly indicating oxidation products from aliphatic precursors (Fig. 4). The factor shows elevated signal intensity during May 8-13, coinciding with regional transport events (Fig. S3-S4 and S4S5). Such aliphatic-dominated spectral patterns associated with transport processes were more prominent in winter observations at this site, showing strong correlations with regional pollutants like PM<sub>2.5</sub>. Combined with its multi-generation oxidation characteristics, these features suggest highly aged air masses of regional origin.

#### 3.4.2 Mixed-MT

This factor exhibits a complex molecular composition with a broad carbon number distribution (C<sub>5</sub>-C<sub>15</sub>), suggesting contributions from multiple precursor classes. While monoterpene-derived dinitrates (C<sub>10</sub>H<sub>16</sub>O<sub>8.9</sub>N<sub>2</sub>, C<sub>10</sub>H<sub>18</sub>O<sub>8</sub>N<sub>2</sub>) dominate the composition and indicate multi-generational oxidation, the presence of a wide range of oxidation products implies the involvement of both biogenic and anthropogenic sources. Notably, the most abundant compounds in R2 are C<sub>x</sub>H<sub>2x-3,2x-5</sub>O<sub>6</sub>N, while in R3, the corresponding species are mainly C<sub>x</sub>H<sub>2x-2,2x-4</sub>O<sub>8</sub>N<sub>2</sub> (Table S12), differing by one HNO<sub>2</sub> group. This pattern closely resembles that observed in the D4-AVOC-IV factor, further supporting the involvement of NO in the formation pathways. The high organic nitrate fraction (84%) further supports this interpretation. Taking the C<sub>10</sub> compounds as an illustrative example, species such as C<sub>10</sub>H<sub>17</sub>NO<sub>5-8</sub> are consistent with OH oxidation products of α- and β-pinene observed in laboratory studies, while C<sub>10</sub>H<sub>18</sub>N<sub>2</sub>O<sub>8,9</sub> are likely formed through subsequent generation reactions. Additionally, the presence of C<sub>10</sub>H<sub>15</sub>NO<sub>5-7</sub> suggests a contribution from O<sub>3</sub>-initiated oxidation pathways. Altogether, these observations imply that this factor reflects a mixture of oxidation processes involving both OH and O<sub>3</sub>, rather than being dominated by a single oxidant or precursor type. (Berndt et al., 2016) Although dominated by monoterpene-derived dinitrates (C10H16O8.9N2, C10H18O8N2), indicating multi-generation oxidation processes, its molecular distribution spans a broad range (C<sub>5</sub>-C<sub>15</sub>), with significant signals observed

across different carbon numbers, suggesting a mixture of oxidation products from various precursors beyond monoterpenes. The lack of distinct diurnal patterns in these mixed precursor contributions suggests either regional background characteristics or potential non-linear processes not fully resolved by PMF analysis.

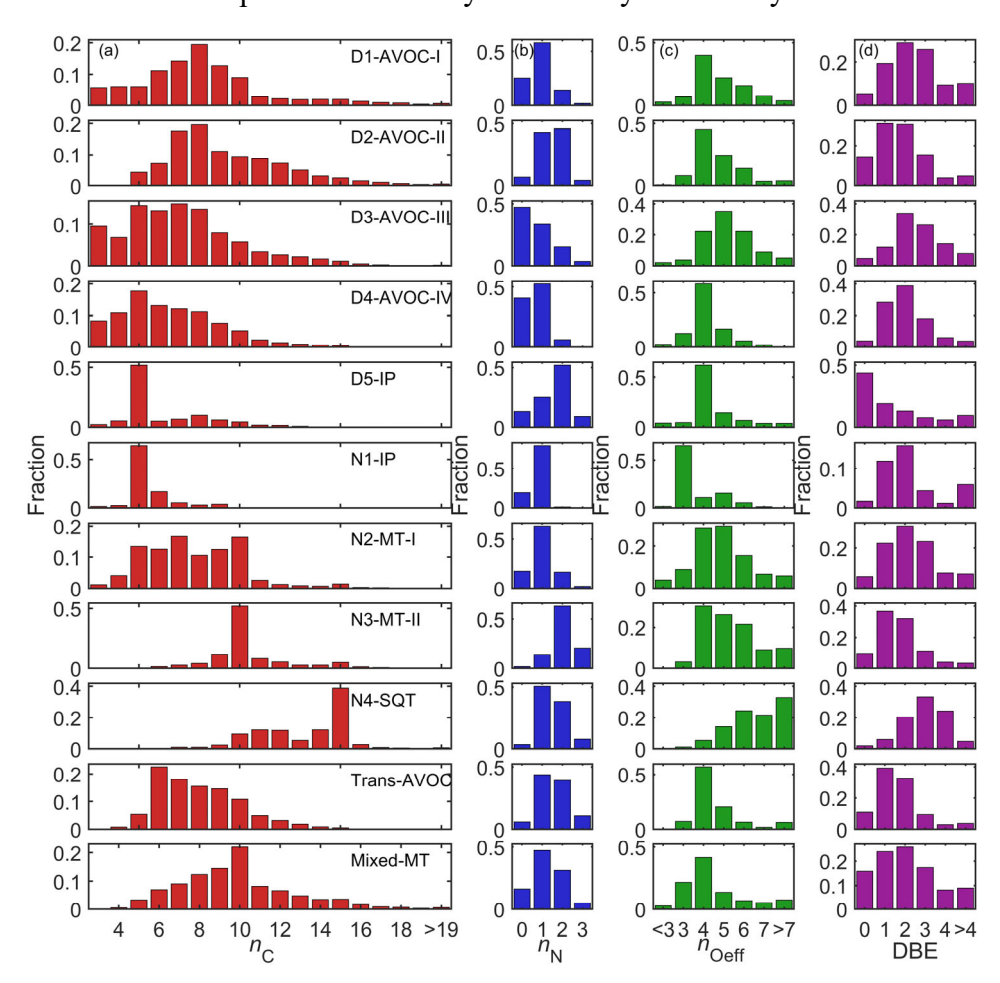


Figure 4. Distribution of (a) the numbers of Carbon ( $n_C$ ), (b) the numbers of Nitrogen ( $n_N$ ), (c) the numbers of Effective Oxygen ( $n_{Oeff}$ ) and (d) double bond equivalents (DBE) of each factor.

# 4 Discussion: from volatility distribution to dynamic chemical processing

The application of multiple sub-range binPMF analysis provides novel insights into the volatility-dependent behavior of OOMs. A systematic examination of the identified factors reveals a clear volatility gradient across the three sub-ranges (R1–R3), which transition progressively from higher to lower volatility compounds (Fig. 5). Specifically, the major products in R1-R3 correspond to semi-volatile organic compounds (SVOCs,  $10^{-0.5} < C^* < 10^{2.5} \ \mu g \ m^{-3}$ ), low-volatility organic compounds (LVOCs,  $10^{-4.5} < C^* < 10^{-0.5} \ \mu g \ m^{-3}$ ), and extremely low-volatility organic compounds (ELVOCs,  $10^{-8.5} < C^* < 10^{-4.5} \ \mu g \ m^{-3}$ ). These classifications, based on saturation vapor concentrations ( $C^*$ ), validate our hypothesis that wider mass ranges inherently encompass greater variations

in OOM volatility, often influenced by differential condensation sinks. The calculation of the saturation vapor concentrations is given in the Supplement. The sub-range approach minimizes such influences, allowing for a more accurate representation of chemical processes responsible for OOM formation.

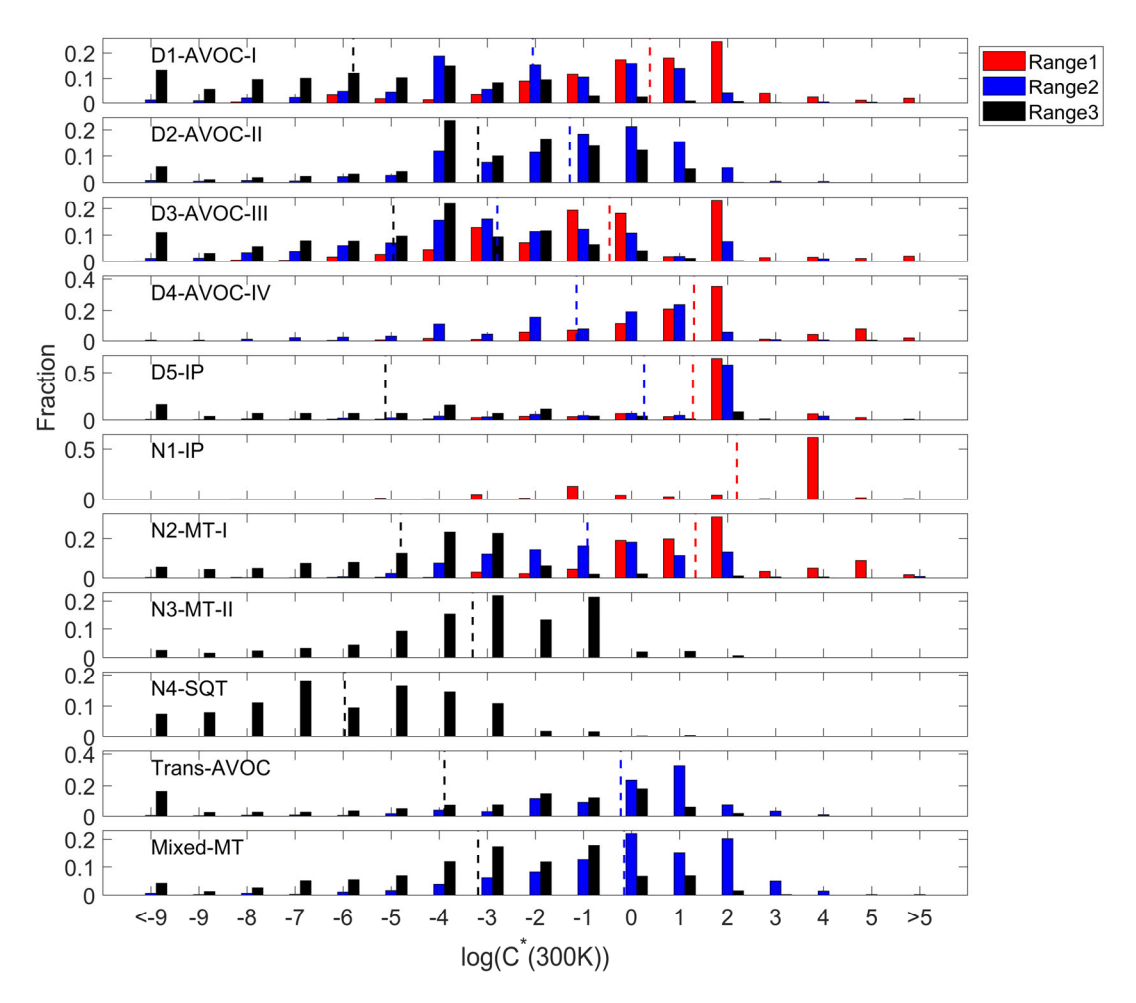


Figure 5. Volatility distribution of each factor at 300K. Columns in red, blue and black represent Range1, Range2 and Range3, respectively. The dotted lines represent the average volatility of the subranges with corresponding colors.

More importantly, this methodology enables us to capture the dynamics driving OOM formation. In contrast to traditional single-range PMF analysis, which assumes static factor profiles, this methodology reveals how chemical conditions and processing pathways evolve over time, reflected by temporal variations in the relative contributions of spectral sub-ranges to individual factors. Specifically, as different sub-ranges are combined, the relative intensities of these ranges fluctuate, demonstrating how variations in chemical reactivity and environmental conditions influence the composition and formation of OOMs. These dynamic observations better represent atmospheric processes, where constantly changing oxidation conditions alter OOM distributions across different volatility ranges. The ability to track these variations in real time allows for a more nuanced understanding of how source and sink processes

interact under different atmospheric conditions. By resolving these dynamics, our method avoids the oversimplification inherent to single-range analyses, which tend to average out temporal variability. Among the identified factors, three (D1-AVOC-I, D3-AVOC-III, and N2-MT-I) are particularly noteworthy as they span all three mass spectral sub-ranges, highlighting both the source and sink processes influencing their formation and distribution under varying atmospheric conditions.



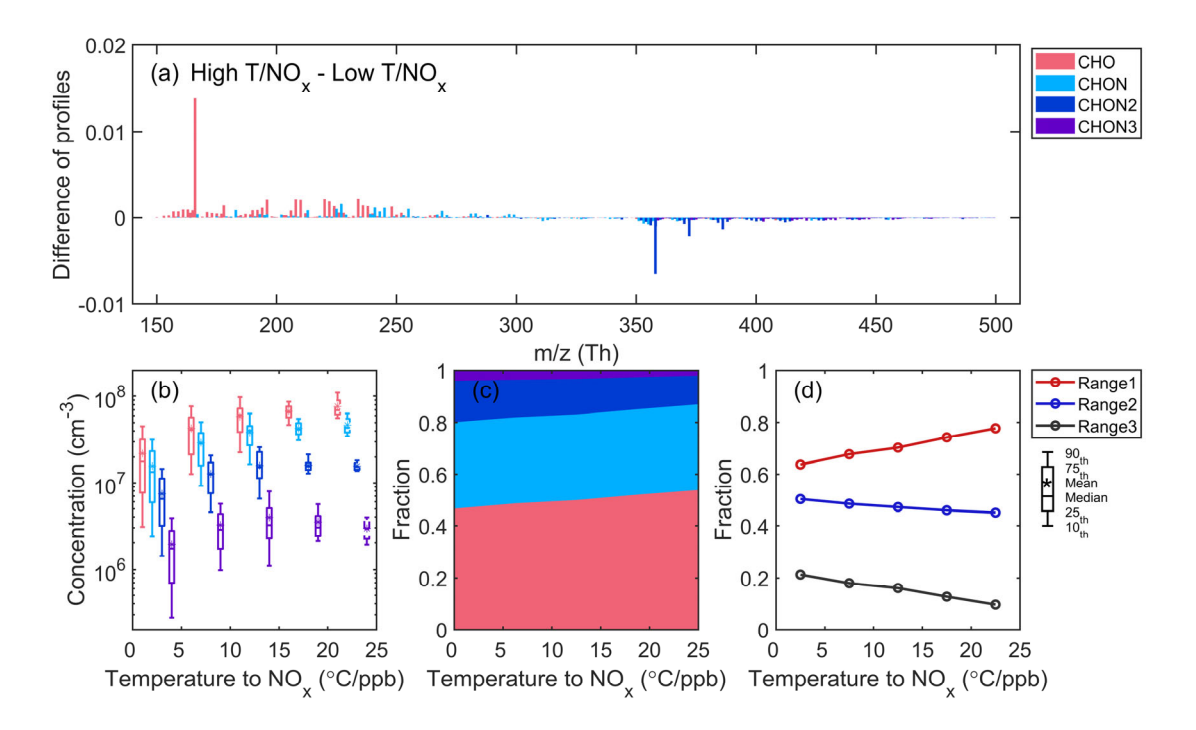


Figure 6. Characteristics of D3-AVOC-III under varying temperature and NOx conditions. (a) Difference between the average mass spectra of D3-AVOC-III under high T/NO<sub>x</sub> (above the upper quartile) and low T/NO<sub>x</sub> (below the lower quartile) conditions. (b) Boxplots of the concentrations of CHO and CHON<sub>x</sub> (x = [1,3]) species binned by T/NO<sub>x</sub> ratio in each 5 °C/ppb interval. Data for T/NO<sub>x</sub> > 20 °C/ppb are represented by dashed box plots owing too few data points. (c) Fractional contributions of CHO and CHON<sub>x</sub> (x = [1,3]) species for different T/NO<sub>x</sub> conditions. (d) Evolution of fractional contributions of three sub-ranges as a function of T/NO<sub>x</sub> ratio.

We examine the D3-AVOC-III factor to demonstrate how varying chemical conditions influence OOM formation pathways. This factor showed limited sensitivity to condensation sink (CS) variations (Fig.  $\frac{$6$10}{$}$ ), suggesting its temporal evolution primarily reflects formation processes rather than loss mechanisms. To systematically investigate its behavior under different chemical environments, we focused on periods with significant daily variations (09:00-21:00 LT) where concentrations exceeded  $1\times10^4$  cm<sup>-3</sup> across all sub-ranges. Given this factor's temperature dependence (Fig.

\$5587), we aimed to examined its impact on chemical composition, particularly the influence on organic nitrate formation, to validate our proposed reaction pathways. While temperature and NO<sub>x</sub> individually influence oxidation chemistry, analyzing them in isolation may obscure their combined effects—especially since NO<sub>x</sub> levels tend to decrease with increasing temperature due to enhanced photochemical activity and atmospheric mixing. -To better isolate the influence of temperature under comparable NO<sub>x</sub> conditions, we adopted the ratio of temperature to NO<sub>x</sub> (T/NO<sub>x</sub>) as a simplified metric. Although this ratio does not represent a physically defined parameter, it serves as a practical index allowing for clearer grouping of data and a more interpretable assessment of compositional differences. Since NO<sub>\*</sub> plays a key role in organic nitrate formation and is typically lower at higher temperatures due to enhanced atmospheric mixing and photochemical activity, using the T/NO<sub>\*</sub> ratio allows us to better isolate the effect of chemical mechanisms on oxidation product distributions. To further explore how temperature to NO<sub>x</sub> (T/NO<sub>x</sub>) conditions influence the composition of this factor, we analyzed the difference between the average mass spectra under high T/NO<sub>x</sub> (above the upper quartile) and low T/NO<sub>x</sub> (below the lower quartile) conditions (Fig. 6a). The results indicate that CHO species contribute more under high temperature and low NO<sub>x</sub> conditions. This pattern suggests that elevated temperatures and lower NO<sub>x</sub> levels promote pathways favoring non-nitrated oxidation products. Concentrations of all species increased with the T/NO<sub>x</sub> ratio (Fig. 6b), indicative of enhanced oxidation processes likely driven by elevated OH concentrations at higher temperatures and moderately reduced NO<sub>x</sub> levels. Interestingly, the relative abundance of product species exhibited distinct patterns within this factor: the fraction of CHO species increased, while that of di- and tri-nitrates decreased as the T/NO<sub>x</sub> ratio increased (Fig. 6c). This trend reflects shifts in RO<sub>2</sub> radical chemistry. Under high NO<sub>x</sub> conditions, RO<sub>2</sub> primarily reacts with NO, and this reaction has two main pathways: formation of RO + NO<sub>2</sub> or organic nitrates (RONO<sub>2</sub>). Previous studies have shown that increasing temperature suppresses the nitrate-forming branch in favor of the RO + NO<sub>2</sub> branch, thus reducing the formation of RONO<sub>2</sub> (Cassanelli et al., 2007; Butkovskaya et al., 2010; Perring et al., 2013)(Cassanelli et al., 2007; Butkovskaya et al., 2010; Perring et al., 2013). This trend reflects shifts in RO<sub>2</sub> radical chemistry—under high NO<sub>\*</sub> conditions, RO2 preferentially reacts with NO, whereas elevated temperatures favor the RO + NO2 channel, reducing the formation of RONO2 from the RO2+ NO reaction. The observed chemical evolution of this factor is largely driven by shifts in the fractional contributions of different sub-ranges (Fig. 6d). The increase in R1's proportion suggests that lower m/z oxidation products (likely associated with CHO species) become more dominant under high T/NO<sub>x</sub> conditions. However, the oxygen number distribution across this factor remained relatively stable, regardless of the T/NO<sub>x</sub> ratio. This observation suggests that our current sub-range resolution may not fully capture autoxidation products, which typically involve the addition of 1–3 molecular oxygen units (O2) and may remain confined to individual sub-ranges. Finer mass spectral resolution could potentially reveal additional insights into the competition between

600

601

602

603

604 605

606

607

608

609

610 611

612

613 614

615616

617

618

619

620

621 622

623

624

625

626

627

628 629

630

631

632633

634

635 636

637

638

639

640



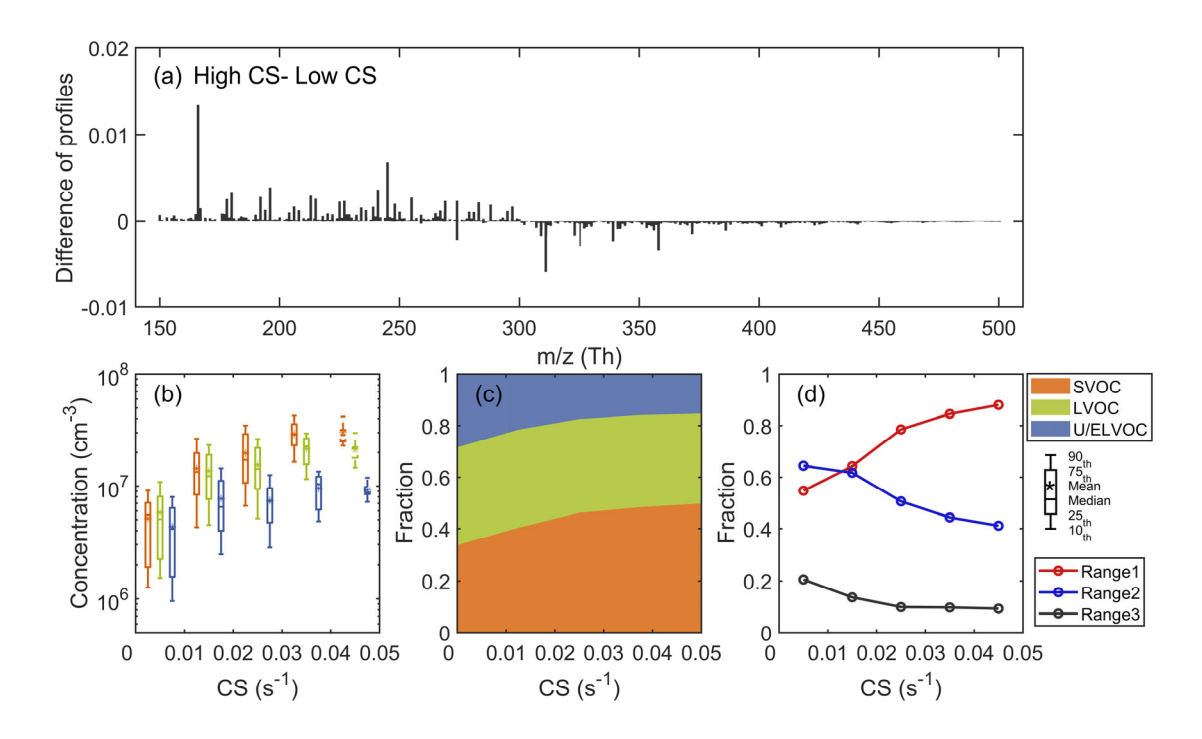


Figure 7. Characteristics of the D1-AVOC-I factor under varying condensation sink (CS) conditions. (a) Difference between the average mass spectra of D1-AVOC-I under high CS (above the upper quartile) and low CS (below the lower quartile) conditions. (b) Boxplots of the concentrations of SVOC, LVOC, and U/ELVOC species binned by CS in each  $0.01~\rm s^{-1}$  interval. Data for CS >  $0.04~\rm s^{-1}$  are represented by dashed box plots owing too few data points. (c) Fractional contributions of SVOC, LVOC, and U/ELVOC species across different CS conditions. (d) Evolution of fractional contributions of three sub-ranges as a function of CS.

Beyond source processes, we also investigated how condensation sink influences the loss mechanisms of these factors, particularly through their volatility-dependent behavior. For this investigation, we focused on D1-AVOC-I and N2-MT-I factors, which exhibited the most pronounced CS dependence (Fig. 7 and Fig. \$7\frac{\text{S11}}{\text{s11}}\)). By analyzing their high-concentration periods (D1: 08:00-16:00 LT; N2: 20:00-04:00 LT), we examined how CS modulates the contributions from species across different volatility classes. By analyzing the difference in average mass spectra between high and low CS conditions (Fig. 7a), we find that higher CS conditions are associated with a depletion of lower-volatility species (LVOC and below) and an enrichment of more volatile compounds (SVOC and above). Our results also reveal that concentrations across all volatility classes initially increase with rising CS (Fig. 7b), a trend attributed to enhanced precursor availability during pollution episodes, as discussed in detail in

our previous analysis. However, this growth pattern exhibits distinct volatilitydependent variations. Lower-volatility species show more pronounced response to CS changes, as they have higher condensation rates onto particles, making them more susceptible to condensational losses under high CS conditions. Consequently, as CS increases, we observe a systematic shift in the relative composition: the fraction of more volatile species increases, while the proportion of lower-volatility compounds decreases (Fig. 7c). This redistribution occurs because when CS values are elevated, the condensation process becomes increasingly competitive with chemical production, particularly for low-volatility species, leading to their preferential depletion from the gas phase. Under extremely high CS conditions, this shift becomes even more pronounced, as condensation onto particles surpasses chemical production, leading to a net decrease in gas-phase concentrations for low-volatility species. This observation aligns with prior theoretical predictions and laboratory findings (Peräkylä et al., 2020), which suggest that under high CS conditions, condensation dominates over chemical formation in shaping the gas-phase abundance of different volatility classes of OOMswhich suggest that condensation processes under high CS conditions act as a controlling mechanism for species partitioning. We analyzed the fractional contributions of different sub-ranges under varying CS conditions. Due to their lower volatility, higher m/z species in R2 and R3 are more susceptible to loss through condensation under high CS, while lower m/z species in R1 (likely SVOCs and LVOCs) are less affected. As a result, the relative contribution of R1 increases with CS, whereas those of R2 and R3 gradually decrease. This trend highlights a volatility-dependent partitioning effect, where enhanced condensation preferentially removes less-volatile compounds from the gas phase under elevated CS conditions, as also reflected by the absolute concentration changes of sub-ranges under increasing CS (Fig. S12). We analyzed the fractional contributions of different sub-ranges under varying CS conditions, and the results indicate that the fraction of R1 species increases significantly with CS, while R2 and R3 exhibit decreasing trends, suggesting that higher CS conditions favor the persistence of lower m/z species, likely corresponding to SVOC and LVOC, while suppressing contributions from higher m/z species associated with ULVOC and ELVOC.

697

698

699700

701

702

703704

705

696

666

667

668

669

670

671

672

673

674

675

676

677 678

679

680

681 682

683

684

685

686 687

688

689

690

691

692 693

694 695

# **5 Conclusions**

In this study, we demonstrated the effectiveness of integrating multiple sub-range mass spectral analysis with binPMF to investigate OOM formation and evolution in the complex urban atmosphere. By leveraging this advanced analytical strategy, we compiled a comprehensive dataset of 2,571 OOM molecules (m/z 150–500 Th, excluding nitrated phenols), significantly enhancing the reliability of high-resolution (HR) peak identification, particularly in higher mass ranges where peak densities become increasingly complex. Importantly, it reduced the dimensionality of complex

atmospheric OOM processes into 11 interpretable factors: five factors from daytime photochemical processes, four from nighttime NO<sub>3</sub>-driven oxidation processes, and two from regional mixed sources. Notably, the analysis achieved the first successful separation of sesquiterpene oxidation products in ambient measurements, previously obscured in traditional full-range analysis due to weak signals and overlapping temporal patterns with other nighttime factors, demonstrating superior source apportionment capability.

Further analyses revealed systematic volatility distributions across different mass ranges, showing a clear transition from SVOCs (m/z 150-300 Th) to LVOCs (m/z 250-400 Th) and ELVOCs (m/z 350-500 Th). This observed volatility-dependent distribution validates the critical importance of accounting for condensation losses in mass spectral analyses and reinforces the effectiveness of our sub-range analytical strategy. Moreover, our method successfully captured the dynamic evolution of OOM composition across different characteristic processes. The observed temporal variations in factor profiles provide a more realistic representation of atmospheric processing, revealing how source and sink processes simultaneously shape OOM composition and distribution - insights that would be obscured in traditional single-range PMF analysis where factor profiles remain static.

Overall, the dynamic chemical insights and improved OOM characterization achieved in this study represent a significant step forward in understanding atmospheric OOM chemistry. This integrated analytical approach offers an integrated framework for future studies, with the improved chemical resolution and volatility-dependent analysis providing a clearer understanding of OOM formation mechanisms. Furthermore, these findings offer valuable constraints for refining atmospheric models of SOA formation and assessing their broader environmental impacts.

- 732 Data availability. Measurement data at the SORPES station, including OOM data and relevant trace gas and aerosol data as well as meteorological data, are available upon
- 734 request from the corresponding author before the SORPES database is open to the
- 735 public.
- 736 Author contribution. WN, YLL and AD designed this research. JY and YLL analyzed
- 737 the data and wrote the manuscript. YLL, WN and CY contributed to the advanced
- writing. YLL conducted the OOM observations. CY, QZ, YYL, DG, CL, CZ and XC
- 739 collected other research materials. All authors participated in the relevant scientific
- 740 discussion and commented on the manuscript.
- *Competing interests.* The authors declare that they have no conflict of interest.
- 742 Acknowledgements. We thank our colleagues and students at the School of Atmospheric
- Sciences at Nanjing University and the SORPES station for their contributions to the
- maintenance of the measurements. We thank the tofTools team for providing tools for

- mass spectrometry analysis.
- 746 Financial support. This work was mainly funded by the National Natural Science
- Foundation of China (NSFC) (42220104006 and 42305119), the Science Fund for
- Distinguished Young Scholars of Jiangsu Province (BK20240067), the Natural Science
- Foundation of Jiangsu Province (BK20230773), the Jiangsu Provincial Collaborative
- 750 Innovation Center of Climate Change, and the Fundamental Research Funds for the
- 751 Central Universities.

753

754

# Reference

- 755 Algrim, L. B. and Ziemann, P. J.: Effect of the Hydroxyl Group on Yields and Composition of
- 756 Organic Aerosol Formed from OH Radical-Initiated Reactions of Alcohols in the Presence of NO<sub>x</sub>,
- 757 ACS Earth Space Chem., 3, 413–423, https://doi.org/10.1021/acsearthspacechem.9b00015, 2019.
- Bianchi, F., Kurtén, T., Riva, M., Mohr, C., Rissanen, M. P., Roldin, P., Berndt, T., Crounse, J. D.,
- Wennberg, P. O., Mentel, T. F., Wildt, J., Junninen, H., Jokinen, T., Kulmala, M., Worsnop, D. R.,
- 760 Thornton, J. A., Donahue, N., Kjaergaard, H. G., and Ehn, M.: Highly Oxygenated Organic
- 761 Molecules (HOM) from Gas-Phase Autoxidation Involving Peroxy Radicals: A Key Contributor to
- 762 Atmospheric Aerosol, Chem. Rev., 119, 3472–3509, https://doi.org/10.1021/acs.chemrev.8b00395,
- 763 2019.
- Butkovskaya, N., Kukui, A., and Le Bras, G.: Pressure and Temperature Dependence of Ethyl
- Nitrate Formation in the C<sub>2</sub> H<sub>5</sub> O<sub>2</sub> + NO Reaction, J. Phys. Chem. A, 114, 956–964,
- 766 https://doi.org/10.1021/jp910003a, 2010.
- 767 Cassanelli, P., Fox, D. J., and Cox, R. A.: Temperature dependence of pentyl nitrate formation
- from the reaction of pentyl peroxy radicals with NO, Phys. Chem. Chem. Phys., 9, 4332,
- 769 https://doi.org/10.1039/b700285h, 2007.
- 770 Chen, Y., Zheng, P., Wang, Z., Pu, W., Tan, Y., Yu, C., Xia, M., Wang, W., Guo, J., Huang, D.,
- Yan, C., Nie, W., Ling, Z., Chen, Q., Lee, S., and Wang, T.: Secondary Formation and Impacts of
- 772 Gaseous Nitro-Phenolic Compounds in the Continental Outflow Observed at a Background Site in
- 773 South China, Environ. Sci. Technol., 56, 6933–6943, https://doi.org/10.1021/acs.est.1c04596, 2022.
- 774 Cheng, X., Chen, Q., Li, Y., Huang, G., Liu, Y., Lu, S., Zheng, Y., Qiu, W., Lu, K., Qiu, X.,
- Bianchi, F., Yan, C., Yuan, B., Shao, M., Wang, Z., Canagaratna, M. R., Zhu, T., Wu, Y., and Zeng,
- 776 L.: Secondary Production of Gaseous Nitrated Phenols in Polluted Urban Environments, Environ.
- 777 Sci. Technol., 55, 4410–4419, https://doi.org/10.1021/acs.est.0c07988, 2021.
- Curtius, J., Heinritzi, M., Beck, L. J., Pöhlker, M. L., Tripathi, N., Krumm, B. E., Holzbeck, P.,
- 779 Nussbaumer, C. M., Hernández Pardo, L., Klimach, T., Barmpounis, K., Andersen, S. T., Bardakov,
- 780 R., Bohn, B., Cecchini, M. A., Chaboureau, J.-P., Dauhut, T., Dienhart, D., Dörich, R., Edtbauer, A.,
- Giez, A., Hartmann, A., Holanda, B. A., Joppe, P., Kaiser, K., Keber, T., Klebach, H., Krüger, O. O.,

- Kürten, A., Mallaun, C., Marno, D., Martinez, M., Monteiro, C., Nelson, C., Ort, L., Raj, S. S.,
- Richter, S., Ringsdorf, A., Rocha, F., Simon, M., Sreekumar, S., Tsokankunku, A., Unfer, G. R.,
- Valenti, I. D., Wang, N., Zahn, A., Zauner-Wieczorek, M., Albrecht, R. I., Andreae, M. O., Artaxo,
- P., Crowley, J. N., Fischer, H., Harder, H., Herdies, D. L., Machado, L. A. T., Pöhlker, C., Pöschl,
- 786 U., Possner, A., Pozzer, A., Schneider, J., Williams, J., and Lelieveld, J.: Isoprene nitrates drive new
- 787 particle formation in Amazon's upper troposphere, Nature, 636, 124-130,
- 788 https://doi.org/10.1038/s41586-024-08192-4, 2024.
- 789 Dada, L., Stolzenburg, D., Simon, M., Fischer, L., Heinritzi, M., Wang, M., Xiao, M., Vogel, A.
- 790 L., Ahonen, L., Amorim, A., Baalbaki, R., Baccarini, A., Baltensperger, U., Bianchi, F., Daellenbach,
- 791 K. R., DeVivo, J., Dias, A., Dommen, J., Duplissy, J., Finkenzeller, H., Hansel, A., He, X.-C.,
- Hofbauer, V., Hoyle, C. R., Kangasluoma, J., Kim, C., Kürten, A., Kvashnin, A., Mauldin, R.,
- Makhmutov, V., Marten, R., Mentler, B., Nie, W., Petäjä, T., Quéléver, L. L. J., Saathoff, H., Tauber,
- 794 C., Tome, A., Molteni, U., Volkamer, R., Wagner, R., Wagner, A. C., Wimmer, D., Winkler, P. M.,
- Yan, C., Zha, Q., Rissanen, M., Gordon, H., Curtius, J., Worsnop, D. R., Lehtipalo, K., Donahue, N.
- 796 M., Kirkby, J., El Haddad, I., and Kulmala, M.: Role of sesquiterpenes in biogenic new particle
- 797 formation, Sci. Adv., 9, eadi5297, https://doi.org/10.1126/sciadv.adi5297, 2023.
- 798 Ding, A., Fu, C. B., Yang, X. Q., Sun, J. N., Zheng, L. F., Xie, Y. N., Herrmann, E., Nie, W.,
- 799 Petäjä, T., Kerminen, V.-M., and Kulmala, M.: Ozone and fine particle in the western Yangtze River
- Delta: an overview of 1 yr data at the SORPES station, Atmospheric Chem. Phys., 13, 5813–5830,
- 801 https://doi.org/10.5194/acp-13-5813-2013, 2013.
- Ding, A., Nie, W., Huang, X., Chi, X., Sun, J., Kerminen, V.-M., Xu, Z., Guo, W., Petäjä, T., Yang,
- 803 X., Kulmala, M., and Fu, C.: Long-term observation of air pollution-weather/climate interactions at
- 804 the SORPES station: a review and outlook, Front. Environ. Sci. Eng., 10, 15,
- 805 https://doi.org/10.1007/s11783-016-0877-3, 2016.
- 806 Ehn, M., Junninen, H., Petäjä, T., Kurtén, T., Kerminen, V.-M., Schobesberger, S., Manninen, H.
- 807 E., Ortega, I. K., Vehkamäki, H., Kulmala, M., and Worsnop, D. R.: Composition and temporal
- 808 behavior of ambient ions in the boreal forest, Atmospheric Chem. Phys., 10, 8513-8530,
- 809 https://doi.org/10.5194/acp-10-8513-2010, 2010.
- 810 Ehn, M., Thornton, J. A., Kleist, E., Sipilä, M., Junninen, H., Pullinen, I., Springer, M., Rubach,
- 811 F., Tillmann, R., Lee, B., Lopez-Hilfiker, F., Andres, S., Acir, I.-H., Rissanen, M., Jokinen, T.,
- 812 Schobesberger, S., Kangasluoma, J., Kontkanen, J., Nieminen, T., Kurtén, T., Nielsen, L. B.,
- Jørgensen, S., Kjaergaard, H. G., Canagaratna, M., Maso, M. D., Berndt, T., Petäjä, T., Wahner, A.,
- Kerminen, V.-M., Kulmala, M., Worsnop, D. R., Wildt, J., and Mentel, T. F.: A large source of low-
- volatility secondary organic aerosol, Nature, 506, 476–479, https://doi.org/10.1038/nature13032,
- 816 2014.
- Gao, L., Song, J., Mohr, C., Huang, W., Vallon, M., Jiang, F., Leisner, T., and Saathoff, H.:
- Kinetics, SOA yields, and chemical composition of secondary organic aerosol from  $\beta$  -
- caryophyllene ozonolysis with and without nitrogen oxides between 213 and 313 K, Atmospheric
- 820 Chem. Phys., 22, 6001–6020, https://doi.org/10.5194/acp-22-6001-2022, 2022.
- 821 Ge, D., Nie, W., Liu, Y., Huang, D. D., Yan, C., Wang, J., Li, Y., Liu, C., Wang, L., Wang, J., Chi,
- X., and Ding, A.: New Insights Into the Sources of Atmospheric Organic Aerosols in East China: A

- 823 Comparison of Online Molecule-Level and Bulk Measurements, J. Geophys. Res. Atmospheres,
- 824 129, e2024JD040768, https://doi.org/10.1029/2024JD040768, 2024.
- Goldman, M. J., Green, W. H., and Kroll, J. H.: Chemistry of Simple Organic Peroxy Radicals
- 826 under Atmospheric through Combustion Conditions: Role of Temperature, Pressure, and NO x
- 827 Level, J. Phys. Chem. A, 125, 10303–10314, https://doi.org/10.1021/acs.jpca.1c07203, 2021.
- 828 Guo, Y., Shen, H., Pullinen, I., Luo, H., Kang, S., Vereecken, L., Fuchs, H., Hallquist, M., Acir,
- 829 I.-H., Tillmann, R., Rohrer, F., Wildt, J., Kiendler-Scharr, A., Wahner, A., Zhao, D., and Mentel, T.
- 830 F.: Identification of highly oxygenated organic molecules and their role in aerosol formation in the
- 831 reaction of limonene with nitrate radical, Atmospheric Chem. Phys., 22, 11323-11346,
- 832 https://doi.org/10.5194/acp-22-11323-2022, 2022a.
- 833 Guo, Y., Yan, C., Liu, Y., Qiao, X., Zheng, F., Zhang, Y., Zhou, Y., Li, C., Fan, X., Lin, Z., Feng,
- 834 Z., Zhang, Y., Zheng, P., Tian, L., Nie, W., Wang, Z., Huang, D., Daellenbach, K. R., Yao, L., Dada,
- 835 L., Bianchi, F., Jiang, J., Liu, Y., Kerminen, V.-M., and Kulmala, M.: Seasonal variation in
- oxygenated organic molecules in urban Beijing and their contribution to secondary organic aerosol,
- 837 Atmospheric Chem. Phys., 22, 10077–10097, https://doi.org/10.5194/acp-22-10077-2022, 2022b.
- Hallquist, M., Wenger, J. C., Baltensperger, U., Rudich, Y., Simpson, D., Claeys, M., Dommen,
- J., Donahue, N. M., George, C., Goldstein, A. H., Hamilton, J. F., Herrmann, H., Hoffmann, T.,
- 840 Iinuma, Y., Jang, M., Jenkin, M. E., Jimenez, J. L., Kiendler-Scharr, A., Maenhaut, W., McFiggans,
- 841 G., Mentel, T. F., Monod, A., Prevot, A. S. H., Seinfeld, J. H., Surratt, J. D., Szmigielski, R., and
- Wildt, J.: The formation, properties and impact of secondary organic aerosol: current and emerging
- issues, Atmos Chem Phys, 2009.
- Heinritzi, M., Simon, M., Steiner, G., Wagner, A. C., Kürten, A., Hansel, A., and Curtius, J.:
- Characterization of the mass-dependent transmission efficiency of a CIMS, Atmos Meas Tech, 2016.
- Heinritzi, M., Dada, L., Simon, M., Stolzenburg, D., Wagner, A. C., Fischer, L., Ahonen, L. R.,
- Amanatidis, S., Baalbaki, R., Baccarini, A., Bauer, P. S., Baumgartner, B., Bianchi, F., Brilke, S.,
- 848 Chen, D., Chiu, R., Dias, A., Dommen, J., Duplissy, J., Finkenzeller, H., Frege, C., Fuchs, C.,
- Garmash, O., Gordon, H., Granzin, M., El Haddad, I., He, X., Helm, J., Hofbauer, V., Hoyle, C. R.,
- Kangasluoma, J., Keber, T., Kim, C., Kürten, A., Lamkaddam, H., Laurila, T. M., Lampilahti, J.,
- Lee, C. P., Lehtipalo, K., Leiminger, M., Mai, H., Makhmutov, V., Manninen, H. E., Marten, R.,
- Mathot, S., Mauldin, R. L., Mentler, B., Molteni, U., Müller, T., Nie, W., Nieminen, T., Onnela, A.,
- Partoll, E., Passananti, M., Petäjä, T., Pfeifer, J., Pospisilova, V., Quéléver, L. L. J., Rissanen, M. P.,
- Rose, C., Schobesberger, S., Scholz, W., Scholze, K., Sipilä, M., Steiner, G., Stozhkov, Y., Tauber,
- 855 C., Tham, Y. J., Vazquez-Pufleau, M., Virtanen, A., Vogel, A. L., Volkamer, R., Wagner, R., Wang,
- M., Weitz, L., Wimmer, D., Xiao, M., Yan, C., Ye, P., Zha, Q., Zhou, X., Amorim, A., Baltensperger,
- U., Hansel, A., Kulmala, M., Tomé, A., Winkler, P. M., Worsnop, D. R., Donahue, N. M., Kirkby,
- 858 J., and Curtius, J.: Molecular understanding of the suppression of new-particle formation by
- 859 isoprene, Atmospheric Chem. Phys., 20, 11809–11821, https://doi.org/10.5194/acp-20-11809-2020,
- 860 2020.
- Hyttinen, N., Kupiainen-Määttä, O., Rissanen, M. P., Muuronen, M., Ehn, M., and Kurtén, T.:
- 862 Modeling the Charging of Highly Oxidized Cyclohexene Ozonolysis Products Using Nitrate-Based
- 863 Chemical Ionization, J. Phys. Chem. A, 119, 6339–6345, https://doi.org/10.1021/acs.jpca.5b01818,

- 864 2015.
- 865 IPCC: Climate Change 2021 The Physical Science Basis: Working Group I Contribution to the
- 866 Sixth Assessment Report of the Intergovernmental Panel on Climate Change, 1st ed., Cambridge
- 867 University Press, https://doi.org/10.1017/9781009157896, 2023.
- Jenkin, M. E., Young, J. C., and Rickard, A. R.: The MCM v3.3.1 degradation scheme for isoprene,
- 869 Atmospheric Chem. Phys., 15, 11433–11459, https://doi.org/10.5194/acp-15-11433-2015, 2015.
- Jimenez, J. L., Canagaratna, M. R., Donahue, N. M., Prevot, A. S. H., Zhang, Q., Kroll, J. H.,
- DeCarlo, P. F., Allan, J. D., Coe, H., Ng, N. L., Aiken, A. C., Docherty, K. S., Ulbrich, I. M.,
- 672 Grieshop, A. P., Robinson, A. L., Duplissy, J., Smith, J. D., Wilson, K. R., Lanz, V. A., Hueglin, C.,
- 873 Sun, Y. L., Tian, J., Laaksonen, A., Raatikainen, T., Rautiainen, J., Vaattovaara, P., Ehn, M., Kulmala,
- M., Tomlinson, J. M., Collins, D. R., Cubison, M. J., E., Dunlea, J., Huffman, J. A., Onasch, T. B.,
- Alfarra, M. R., Williams, P. I., Bower, K., Kondo, Y., Schneider, J., Drewnick, F., Borrmann, S.,
- Weimer, S., Demerjian, K., Salcedo, D., Cottrell, L., Griffin, R., Takami, A., Miyoshi, T.,
- Hatakeyama, S., Shimono, A., Sun, J. Y., Zhang, Y. M., Dzepina, K., Kimmel, J. R., Sueper, D.,
- Jayne, J. T., Herndon, S. C., Trimborn, A. M., Williams, L. R., Wood, E. C., Middlebrook, A. M.,
- 879 Kolb, C. E., Baltensperger, U., and Worsnop, D. R.: Evolution of Organic Aerosols in the
- 880 Atmosphere, Science, 326, 1525–1529, https://doi.org/10.1126/science.1180353, 2009.
- Jokinen, T., Sipilä, M., Junninen, H., Ehn, M., Lönn, G., Hakala, J., Petäjä, T., Mauldin, R. L.,
- 882 Kulmala, M., and Worsnop, D. R.: Atmospheric sulphuric acid and neutral cluster measurements
- 883 using CI-APi-TOF, Atmospheric Chem. Phys., 12, 4117–4125, https://doi.org/10.5194/acp-12-
- 884 4117-2012, 2012.
- Jokinen, T., Berndt, T., Makkonen, R., Kerminen, V.-M., Junninen, H., Paasonen, P., Stratmann,
- 886 F., Herrmann, H., Guenther, A. B., Worsnop, D. R., Kulmala, M., Ehn, M., and Sipilä, M.:
- 887 Production of extremely low volatile organic compounds from biogenic emissions: Measured yields
- 888 and atmospheric implications, Proc. Natl. Acad. Sci., 112, 7123-7128,
- https://doi.org/10.1073/pnas.1423977112, 2015.
- Junninen, H., Ehn, M., Petäjä, T., Luosujärvi, L., Kotiaho, T., Kostiainen, R., Rohner, U., Gonin,
- 891 M., Fuhrer, K., Kulmala, M., and Worsnop, D. R.: A high-resolution mass spectrometer to measure
- 892 atmospheric ion composition, Atmospheric Meas. Tech., 3, 1039–1053,
- 893 https://doi.org/10.5194/amt-3-1039-2010, 2010.
- 894 Kenagy, H. S., Heald, C. L., Tahsini, N., Goss, M. B., and Kroll, J. H.: Can we achieve
- 895 atmospheric chemical environments in the laboratory? An integrated model-measurement approach
- to chamber SOA studies, CENCEVNCES, 2024.
- 897 Kürten, A., Rondo, L., Ehrhart, S., and Curtius, J.: Calibration of a Chemical Ionization Mass
- 898 Spectrometer for the Measurement of Gaseous Sulfuric Acid, J. Phys. Chem. A, 116, 6375–6386,
- 899 https://doi.org/10.1021/jp212123n, 2012.
- Lee, B. H., Lopez-Hilfiker, F. D., Mohr, C., Kurtén, T., Worsnop, D. R., and Thornton, J. A.: An
- 901 Iodide-Adduct High-Resolution Time-of-Flight Chemical-Ionization Mass Spectrometer:
- 902 Application to Atmospheric Inorganic and Organic Compounds, Environ. Sci. Technol., 48, 6309–
- 903 6317, https://doi.org/10.1021/es500362a, 2014.

- Lim, S. S., Vos, T., Flaxman, A. D., Danaei, G., Shibuya, K., Adair-Rohani, H., AlMazroa, M. A.,
- Amann, M., Anderson, H. R., Andrews, K. G., Aryee, M., Atkinson, C., Bacchus, L. J., Bahalim, A.
- N., Balakrishnan, K., Balmes, J., Barker-Collo, S., Baxter, A., Bell, M. L., Blore, J. D., Blyth, F.,
- 907 Bonner, C., Borges, G., Bourne, R., Boussinesq, M., Brauer, M., Brooks, P., Bruce, N. G.,
- 908 Brunekreef, B., Bryan-Hancock, C., Bucello, C., Buchbinder, R., Bull, F., Burnett, R. T., Byers, T.
- 909 E., Calabria, B., Carapetis, J., Carnahan, E., Chafe, Z., Charlson, F., Chen, H., Chen, J. S., Cheng,
- 910 A. T.-A., Child, J. C., Cohen, A., Colson, K. E., Cowie, B. C., Darby, S., Darling, S., Davis, A.,
- Degenhardt, L., Dentener, F., Des Jarlais, D. C., Devries, K., Dherani, M., Ding, E. L., Dorsey, E.
- 912 R., Driscoll, T., Edmond, K., Ali, S. E., Engell, R. E., Erwin, P. J., Fahimi, S., Falder, G., Farzadfar,
- 913 F., Ferrari, A., Finucane, M. M., Flaxman, S., Fowkes, F. G. R., Freedman, G., Freeman, M. K.,
- Gakidou, E., Ghosh, S., Giovannucci, E., Gmel, G., Graham, K., Grainger, R., Grant, B., Gunnell,
- D., Gutierrez, H. R., Hall, W., Hoek, H. W., Hogan, A., Hosgood, H. D., Hoy, D., Hu, H., Hubbell,
- B. J., Hutchings, S. J., Ibeanusi, S. E., Jacklyn, G. L., Jasrasaria, R., Jonas, J. B., Kan, H., Kanis, J.
- 917 A., Kassebaum, N., Kawakami, N., Khang, Y.-H., Khatibzadeh, S., Khoo, J.-P., et al.: A comparative
- 918 risk assessment of burden of disease and injury attributable to 67 risk factors and risk factor clusters
- 919 in 21 regions, 1990–2010: a systematic analysis for the Global Burden of Disease Study 2010, The
- 920 Lancet, 380, 2224–2260, https://doi.org/10.1016/S0140-6736(12)61766-8, 2012.
- Liu, Y., Nie, W., Xu, Z., Wang, T., Wang, R., Li, Y., Wang, L., Chi, X., and Ding, A.: Semi-
- 922 quantitative understanding of source contribution to nitrous acid (HONO) based on 1 year of
- ontinuous observation at the SORPES station in eastern China, Atmos Chem Phys, 2019.
- 924 Liu, Y., Nie, W., Li, Y., Ge, D., Liu, C., Xu, Z., Chen, L., Wang, T., Wang, L., Sun, P., Qi, X.,
- Wang, J., Xu, Z., Yuan, J., Yan, C., Zhang, Y., Huang, D., Wang, Z., Donahue, N. M., Worsnop, D.,
- 926 Chi, X., Ehn, M., and Ding, A.: Formation of condensable organic vapors from anthropogenic and
- 927 biogenic volatile organic compounds (VOCs) is strongly perturbed by NOx in eastern China,
- 928 Atmospheric Chem. Phys., 21, 14789–14814, https://doi.org/10.5194/acp-21-14789-2021, 2021.
- 929 Liu, Y., Liu, C., Nie, W., Li, Y., Ge, D., Chen, L., Zhu, C., Wang, L., Zhang, Y., Liu, T., Qi, X.,
- 930 Wang, J., Huang, D., Wang, Z., Yan, C., Chi, X., and Ding, A.: Exploring condensable organic
- vapors and their co-occurrence with PM 2.5 and O 3 in winter in Eastern China, Environ. Sci.
- 932 Atmospheres, 3, 282–297, https://doi.org/10.1039/D2EA00143H, 2023.
- 933 Liu, Y., Nie, W., Qi, X., Li, Y., Xu, T., Liu, C., Ge, D., Chen, L., Niu, G., Wang, J., Yang, L.,
- 934 Wang, L., Zhu, C., Wang, J., Zhang, Y., Liu, T., Zha, Q., Yan, C., Ye, C., Zhang, G., Hu, R., Huang,
- 935 R.-J., Chi, X., Zhu, T., and Ding, A.: The Pivotal Role of Heavy Terpenes and Anthropogenic
- 936 Interactions in New Particle Formation on the Southeastern Qinghai-Tibet Plateau, Environ. Sci.
- 937 Technol., acs.est.4c04112, https://doi.org/10.1021/acs.est.4c04112, 2024.
- Luo, H., Vereecken, L., Shen, H., Kang, S., Pullinen, I., Hallquist, M., Fuchs, H., Wahner, A.,
- 939 Kiendler-Scharr, A., Mentel, T. F., and Zhao, D.: Formation of highly oxygenated organic molecules
- 940 from the oxidation of limonene by OH radical: significant contribution of H-abstraction pathway,
- 941 Atmospheric Chem. Phys., 23, 7297–7319, https://doi.org/10.5194/acp-23-7297-2023, 2023.
- Massoli, P., Stark, H., Canagaratna, M. R., Krechmer, J. E., Xu, L., Ng, N. L., Mauldin, R. L. I.,
- 943 Yan, C., Kimmel, J., Misztal, P. K., Jimenez, J. L., Jayne, J. T., and Worsnop, D. R.: Ambient
- 944 Measurements of Highly Oxidized Gas-Phase Molecules during the Southern Oxidant and Aerosol

- 945 Study (SOAS) 2013, ACS Earth Space Chem., 2, 653–672,
- 946 https://doi.org/10.1021/acsearthspacechem.8b00028, 2018.
- 947 McFiggans, G., Mentel, T. F., Wildt, J., Pullinen, I., Kang, S., Kleist, E., Schmitt, S., Springer,
- 948 M., Tillmann, R., Wu, C., Zhao, D., Hallquist, M., Faxon, C., Le Breton, M., Hallquist, Å. M.,
- 949 Simpson, D., Bergström, R., Jenkin, M. E., Ehn, M., Thornton, J. A., Alfarra, M. R., Bannan, T. J.,
- 950 Percival, C. J., Priestley, M., Topping, D., and Kiendler-Scharr, A.: Secondary organic aerosol
- reduced by mixture of atmospheric vapours, Nature, 565, 587–593, https://doi.org/10.1038/s41586-
- 952 018-0871-y, 2019.
- Mohr, C., Thornton, J. A., Heitto, A., Lopez-Hilfiker, F. D., Lutz, A., Riipinen, I., Hong, J.,
- Donahue, N. M., Hallquist, M., Petäjä, T., Kulmala, M., and Yli-Juuti, T.: Molecular identification
- 955 of organic vapors driving atmospheric nanoparticle growth, Nat. Commun., 10, 4442,
- 956 https://doi.org/10.1038/s41467-019-12473-2, 2019.
- 957 Molteni, U., Bianchi, F., Klein, F., El Haddad, I., Frege, C., Rossi, M. J., Dommen, J., and
- 958 Baltensperger, U.: Formation of highly oxygenated organic molecules from aromatic compounds,
- 959 Atmospheric Chem. Phys., 18, 1909–1921, https://doi.org/10.5194/acp-18-1909-2018, 2018.
- Newland, M. J., Bryant, D. J., Dunmore, R. E., Bannan, T. J., Acton, W. J. F., Langford, B.,
- Hopkins, J. R., Squires, F. A., Dixon, W., Drysdale, W. S., Ivatt, P. D., Evans, M. J., Edwards, P. M.,
- Whalley, L. K., Heard, D. E., Slater, E. J., Woodward-Massey, R., Ye, C., Mehra, A., Worrall, S. D.,
- Bacak, A., Coe, H., Percival, C. J., Hewitt, C. N., Lee, J. D., Cui, T., Surratt, J. D., Wang, X., Lewis,
- A. C., Rickard, A. R., and Hamilton, J. F.: Low-NO atmospheric oxidation pathways in a polluted
- 965 megacity, Atmospheric Chem. Phys., 21, 1613–1625, https://doi.org/10.5194/acp-21-1613-2021,
- 966 2021.
- 967 Nie, W., Ding, A. J., Xie, Y. N., Xu, Z., Mao, H., Kerminen, V.-M., Zheng, L. F., Qi, X. M., Huang,
- 968 X., Yang, X.-Q., Sun, J. N., Herrmann, E., Petäjä, T., Kulmala, M., and Fu, C. B.: Influence of
- 969 biomass burning plumes on HONO chemistry in eastern China, Atmospheric Chem. Phys., 15,
- 970 1147–1159, https://doi.org/10.5194/acp-15-1147-2015, 2015.
- 971 Nie, W., Yan, C., Huang, D. D., Wang, Z., Liu, Y., Qiao, X., Guo, Y., Tian, L., Zheng, P., Xu, Z.,
- Li, Y., Xu, Z., Qi, X., Sun, P., Wang, J., Zheng, F., Li, X., Yin, R., Dallenbach, K. R., Bianchi, F.,
- Petäjä, T., Zhang, Y., Wang, M., Schervish, M., Wang, S., Qiao, L., Wang, Q., Zhou, M., Wang, H.,
- 974 Yu, C., Yao, D., Guo, H., Ye, P., Lee, S., Li, Y. J., Liu, Y., Chi, X., Kerminen, V.-M., Ehn, M.,
- 975 Donahue, N. M., Wang, T., Huang, C., Kulmala, M., Worsnop, D., Jiang, J., and Ding, A.: Secondary
- organic aerosol formed by condensing anthropogenic vapours over China's megacities, Nat. Geosci.,
- 977 15, 255–261, https://doi.org/10.1038/s41561-022-00922-5, 2022.
- Nie, W., Yan, C., Yang, L., Roldin, P., Liu, Y., Vogel, A. L., Molteni, U., Stolzenburg, D.,
- 979 Finkenzeller, H., Amorim, A., Bianchi, F., Curtius, J., Dada, L., Draper, D. C., Duplissy, J., Hansel,
- 980 A., He, X.-C., Hofbauer, V., Jokinen, T., Kim, C., Lehtipalo, K., Nichman, L., Mauldin, R. L.,
- 981 Makhmutov, V., Mentler, B., Mizelli-Ojdanic, A., Petäjä, T., Quéléver, L. L. J., Schallhart, S., Simon,
- 982 M., Tauber, C., Tomé, A., Volkamer, R., Wagner, A. C., Wagner, R., Wang, M., Ye, P., Li, H., Huang,
- 983 W., Qi, X., Lou, S., Liu, T., Chi, X., Dommen, J., Baltensperger, U., El Haddad, I., Kirkby, J.,
- 984 Worsnop, D., Kulmala, M., Donahue, N. M., Ehn, M., and Ding, A.: NO at low concentration can
- enhance the formation of highly oxygenated biogenic molecules in the atmosphere, Nat. Commun.,

- 986 14, 3347, https://doi.org/10.1038/s41467-023-39066-4, 2023.
- 987 Orlando, J. J. and Tyndall, G. S.: Laboratory studies of organic peroxy radical chemistry: an
- overview with emphasis on recent issues of atmospheric significance, Chem. Soc. Rev., 41, 6294,
- 989 https://doi.org/10.1039/c2cs35166h, 2012.
- 990 Peng, Z. and Jimenez, J. L.: Radical chemistry in oxidation flow reactors for atmospheric
- 991 chemistry research, Chem. Soc. Rev., 49, 2570–2616, https://doi.org/10.1039/C9CS00766K, 2020.
- 992 Peräkylä, O., Riva, M., Heikkinen, L., Quéléver, L., Roldin, P., and Ehn, M.: Experimental
- 993 investigation into the volatilities of highly oxygenated organic molecules (HOMs), Atmospheric
- 994 Chem. Phys., 20, 649–669, https://doi.org/10.5194/acp-20-649-2020, 2020.
- Perring, A. E., Pusede, S. E., and Cohen, R. C.: An Observational Perspective on the Atmospheric
- 996 Impacts of Alkyl and Multifunctional Nitrates on Ozone and Secondary Organic Aerosol, Chem.
- 997 Rev., 113, 5848–5870, https://doi.org/10.1021/cr300520x, 2013.
- 998 Riccobono, F., Schobesberger, S., Scott, C. E., Dommen, J., Ortega, I. K., Rondo, L., Almeida, J.,
- 999 Amorim, A., Bianchi, F., Breitenlechner, M., David, A., Downard, A., Dunne, E. M., Duplissy, J.,
- 1000 Ehrhart, S., Flagan, R. C., Franchin, A., Hansel, A., Junninen, H., Kajos, M., Keskinen, H., Kupc,
- 1001 A., Kürten, A., Kvashin, A. N., Laaksonen, A., Lehtipalo, K., Makhmutov, V., Mathot, S., Nieminen,
- T., Onnela, A., Petäjä, T., Praplan, A. P., Santos, F. D., Schallhart, S., Seinfeld, J. H., Sipilä, M.,
- Spracklen, D. V., Stozhkov, Y., Stratmann, F., Tomé, A., Tsagkogeorgas, G., Vaattovaara, P.,
- Viisanen, Y., Vrtala, A., Wagner, P. E., Weingartner, E., Wex, H., Wimmer, D., Carslaw, K. S.,
- 1005 Curtius, J., Donahue, N. M., Kirkby, J., Kulmala, M., Worsnop, D. R., and Baltensperger, U.:
- 1006 Oxidation Products of Biogenic Emissions Contribute to Nucleation of Atmospheric Particles,
- 1007 Science, 344, 717–721, https://doi.org/10.1126/science.1243527, 2014.
- 1008 Richters, S., Herrmann, H., and Berndt, T.: Highly Oxidized RO<sub>2</sub> Radicals and Consecutive
- 1009 Products from the Ozonolysis of Three Sesquiterpenes, Environ. Sci. Technol., 50, 2354–2362,
- 1010 https://doi.org/10.1021/acs.est.5b05321, 2016.
- Riva, M., Rantala, P., Krechmer, J. E., Peräkylä, O., Zhang, Y., Heikkinen, L., Garmash, O., Yan,
- 1012 C., Kulmala, M., Worsnop, D., and Ehn, M.: Evaluating the performance of five different chemical
- 1013 ionization techniques for detecting gaseous oxygenated organic species, Atmospheric Meas. Tech.,
- 1014 12, 2403–2421, https://doi.org/10.5194/amt-12-2403-2019, 2019.
- Shen, H., Zhao, D., Pullinen, I., Kang, S., Vereecken, L., Fuchs, H., Acir, I.-H., Tillmann, R.,
- 1016 Rohrer, F., Wildt, J., Kiendler-Scharr, A., Wahner, A., and Mentel, T. F.: Highly Oxygenated Organic
- 1017 Nitrates Formed from NO <sub>3</sub> Radical-Initiated Oxidation of β-Pinene, Environ. Sci. Technol., 55,
- 1018 15658–15671, https://doi.org/10.1021/acs.est.1c03978, 2021.
- 1019 Shiraiwa, M., Ueda, K., Pozzer, A., Lammel, G., Kampf, C. J., Fushimi, A., Enami, S., Arangio,
- 1020 A. M., Fröhlich-Nowoisky, J., Fujitani, Y., Furuyama, A., Lakey, P. S. J., Lelieveld, J., Lucas, K.,
- 1021 Morino, Y., Pöschl, U., Takahama, S., Takami, A., Tong, H., Weber, B., Yoshino, A., and Sato, K.:
- 1022 Aerosol Health Effects from Molecular to Global Scales, Env. Sci Technol, 2017.
- 1023 Song, K., Guo, S., Wang, H., Yu, Y., Wang, H., Tang, R., Xia, S., Gong, Y., Wan, Z., Lv, D., Tan,
- 1024 R., Zhu, W., Shen, R., Li, X., Yu, X., Chen, S., Zeng, L., and Huang, X.: Measurement report: Online

- measurement of gas-phase nitrated phenols utilizing a CI-LToF-MS: primary sources and secondary
- 1026 formation, Atmospheric Chem. Phys., 21, 7917–7932, https://doi.org/10.5194/acp-21-7917-2021,
- 1027 2021.
- Takeuchi, M., Berkemeier, T., Eris, G., and Ng, N. L.: Non-linear effects of secondary organic
- 1029 aerosol formation and properties in multi-precursor systems, Nat. Commun., 13, 7883,
- 1030 https://doi.org/10.1038/s41467-022-35546-1, 2022.
- 1031 Tian, L., Huang, D. D., Li, Y. J., Yan, C., Nie, W., Wang, Z., Wang, Q., Qiao, L., Zhou, M., Zhu,
- S., Liu, Y., Guo, Y., Qiao, X., Zheng, P., Jing, S., Lou, S., Wang, H., and Huang, C.: Enigma of
- 1033 Urban Gaseous Oxygenated Organic Molecules: Precursor Type, Role of NO x , and Degree of
- Oxygenation, Environ. Sci. Technol., 57, 64–75, https://doi.org/10.1021/acs.est.2c05047, 2023.
- 1035 Tröstl, J., Chuang, W. K., Gordon, H., Heinritzi, M., Molteni, U., Frege, C., Bianchi, F., Wagner,
- 1036 R., Simon, M., Lehtipalo, K., Williamson, C., Craven, J. S., Duplissy, J., Bernhammer, A.-K.,
- Breitenlechner, M., Brilke, S., Dias, A., Ehrhart, S., Flagan, R. C., Franchin, A., Fuchs, C., Guida,
- 1038 R., Gysel, M., Hansel, A., Hoyle, C. R., Jokinen, T., Junninen, H., Kangasluoma, J., Keskinen, H.,
- Kim, J., Krapf, M., Kürten, A., Laaksonen, A., Lawler, M., Leiminger, M., Mathot, S., Möhler, O.,
- Nieminen, T., Onnela, A., Petäjä, T., Piel, F. M., Miettinen, P., Rissanen, M. P., Rondo, L., Sarnela,
- N., Schobesberger, S., Sengupta, K., Sipilä, M., Smith, J. N., Steiner, G., Tomè, A., Virtanen, A.,
- Wagner, A. C., Weingartner, E., Wimmer, D., Winkler, P. M., Carslaw, K. S., Curtius, J., Dommen,
- J., Kirkby, J., Kulmala, M., Riipinen, I., Worsnop, D. R., Donahue, N. M., and Baltensperger, U.:
- The role of low-volatility organic compounds in initial particle growth in the atmosphere, Nature,
- 1045 https://doi.org/10.1038/nature18271, 2016.
- Tsiligiannis, E., Hammes, J., Salvador, C., Mentel, T., and Hallquist, M.: Effect of NOx on 1,3,5-
- 1047 trimethylbenzene (TMB) oxidation product distribution and particle formation, Atmospheric Chem.
- 1048 Phys., 19, 15073–15086, https://doi.org/10.5194/ACP-19-15073-2019, 2019.
- Ulbrich, I. M., Canagaratna, M. R., Zhang, Q., Worsnop, D. R., and Jimenez, J. L.: Interpretation
- of organic components from Positive Matrix Factorization of aerosol mass spectrometric data,
- 1051 Atmos Chem Phys, 2009.
- 1052 Wang, J., Nie, W., Cheng, Y., Shen, Y., Chi, X., Wang, J., Huang, X., Xie, Y., Sun, P., Xu, Z., Qi,
- 1053 X., Su, H., and Ding, A.: Light absorption of brown carbon in eastern China based on 3-year multi-
- 1054 wavelength aerosol optical property observations and an improved absorption Ångström exponent
- segregation method, Atmos Chem Phys, 2018.
- Wang, Y., Mehra, A., Krechmer, J., Yang, G., Hu, X., Lu, Y., Lambe, A., Canagaratna, M., Chen,
- 1057 J., Worsnop, D., Coe, H., and Wang, L.: Oxygenated products formed from OH-initiated reactions
- 1058 of trimethylbenzene: autoxidation and accretion, Atmospheric Chem. Phys., null, null,
- 1059 https://doi.org/10.5194/acp-2020-165, 2020.
- Wang, Z., Ehn, M., Rissanen, M., Garmash, O., Quéléver, L., Xing, L., Monge-Palacios, M.,
- Rantala, P., Donahue, N., Berndt, T., and Sarathy, S. M.: Efficient alkane oxidation under
- 1062 combustion engine and atmospheric conditions, Commun. Chem., 4, null,
- 1063 https://doi.org/10.1038/s42004-020-00445-3, 2021.
- 1064 Xu, Z. N., Nie, W., Liu, Y. L., Sun, P., Huang, D. D., Yan, C., Krechmer, J., Ye, P. L., Xu, Z., Qi,

- 1065 X. M., Zhu, C. J., Li, Y. Y., Wang, T. Y., Wang, L., Huang, X., Tang, R. Z., Guo, S., Xiu, G. L., Fu,
- 1066 Q. Y., Worsnop, D., Chi, X. G., and Ding, A. J.: Multifunctional Products of Isoprene Oxidation in
- Polluted Atmosphere and Their Contribution to SOA, Geophys. Res. Lett., 48, e2020GL089276,
- 1068 https://doi.org/10.1029/2020GL089276, 2021.
- Yan, C., Nie, W., Äijälä, M., Rissanen, M. P., Canagaratna, M. R., Massoli, P., Junninen, H.,
- Jokinen, T., Sarnela, N., Häme, S. A. K., Schobesberger, S., Canonaco, F., Yao, L., Prévôt, A. S. H.,
- 1071 Petäjä, T., Kulmala, M., Sipilä, M., Worsnop, D. R., and Ehn, M.: Source characterization of highly
- 1072 oxidized multifunctional compounds in a boreal forest environment using positive matrix
- 1073 factorization, Atmospheric Chem. Phys., 16, 12715–12731, https://doi.org/10.5194/acp-16-12715-
- 1074 2016, 2016.
- 1075 Ye, C., Yuan, B., Lin, Y., Wang, Z., Hu, W., Li, T., Chen, W., Wu, C., Wang, C., Huang, S., Qi, J.,
- Wang, B., Wang, C., Song, W., Wang, X., Zheng, E., Krechmer, J. E., Ye, P., Zhang, Z., Wang, X.,
- Worsnop, D. R., and Shao, M.: Chemical characterization of oxygenated organic compounds in the
- gas phase and particle phase using iodide CIMS with FIGAERO in urban air, Atmospheric Chem.
- 1079 Phys., 21, 8455–8478, https://doi.org/10.5194/acp-21-8455-2021, 2021.
- 1080 Yuan, Y., Chen, X., Cai, R., Li, X., Li, Y., Yin, R., Li, D., Yan, C., Liu, Y., He, K., Kulmala, M.,
- and Jiang, J.: Resolving Atmospheric Oxygenated Organic Molecules in Urban Beijing Using
- 1082 Online Ultrahigh-Resolution Chemical Ionization Mass Spectrometry, Environ. Sci. Technol., 58,
- 1083 17777–17785, https://doi.org/10.1021/acs.est.4c04214, 2024.
- Zaytsev, A., Koss, A. R., Breitenlechner, M., Krechmer, J. E., Nihill, K. J., Lim, C. Y., Rowe, J.
- 1085 C., Cox, J. L., Moss, J., Roscioli, J. R., Canagaratna, M. R., Worsnop, D. R., Kroll, J. H., and Keutsch,
- 1086 F. N.: Mechanistic study of the formation of ring-retaining and ring-opening products from the
- 1087 oxidation of aromatic compounds under urban atmospheric conditions, Atmospheric Chem. Phys.,
- 1088 19, 15117–15129, https://doi.org/10.5194/acp-19-15117-2019, 2019.
- Zha, Q., Aliaga, D., Krejci, R., Sinclair, V. A., Wu, C., Ciarelli, G., Scholz, W., Heikkinen, L.,
- 1090 Partoll, E., Gramlich, Y., Huang, W., Leiminger, M., Enroth, J., Peräkylä, O., Cai, R., Chen, X.,
- 1091 Koenig, A. M., Velarde, F., Moreno, I., Petäjä, T., Artaxo, P., Laj, P., Hansel, A., Carbone, S.,
- 1092 Kulmala, M., Andrade, M., Worsnop, D., Mohr, C., and Bianchi, F.: Oxidized organic molecules in
- 1093 the tropical free troposphere over Amazonia, Natl. Sci. Rev., 11, nwad138,
- 1094 https://doi.org/10.1093/nsr/nwad138, 2023.
- Zhang, Q., Jimenez, J. L., Canagaratna, M. R., Allan, J. D., Coe, H., Ulbrich, I., Alfarra, M. R.,
- Takami, A., Middlebrook, A. M., Sun, Y. L., Dzepina, K., Dunlea, E., Docherty, K., DeCarlo, P. F.,
- 1097 Salcedo, D., Onasch, T., Jayne, J. T., Miyoshi, T., Shimono, A., Hatakeyama, S., Takegawa, N.,
- 1098 Kondo, Y., Schneider, J., Drewnick, F., Borrmann, S., Weimer, S., Demerjian, K., Williams, P.,
- 1099 Bower, K., Bahreini, R., Cottrell, L., Griffin, R. J., Rautiainen, J., Sun, J. Y., Zhang, Y. M., and
- 1100 Worsnop, D. R.: Ubiquity and dominance of oxygenated species in organic aerosols in
- anthropogenically-influenced Northern Hemisphere midlatitudes, Geophys. Res. Lett., 34,
- 1102 https://doi.org/10.1029/2007GL029979, 2007.
- Zhang, Q., Jimenez, J. L., Canagaratna, M. R., Ulbrich, I. M., Ng, N. L., Worsnop, D. R., and
- 1104 Sun, Y.: Understanding atmospheric organic aerosols via factor analysis of aerosol mass
- spectrometry: a review, Anal. Bioanal. Chem., 401, 3045-3067, https://doi.org/10.1007/s00216-

- 1106 011-5355-y, 2011.
- Zhang, Y., Peräkylä, O., Yan, C., Heikkinen, L., Äijälä, M., Daellenbach, K. R., Zha, Q., Riva,
- 1108 M., Garmash, O., Junninen, H., Paatero, P., Worsnop, D., and Ehn, M.: A novel approach for simple
- statistical analysis of high-resolution mass spectra, Atmospheric Meas. Tech., 12, 3761–3776,
- 1110 https://doi.org/10.5194/amt-12-3761-2019, 2019.
- Zhang, Y., Peräkylä, O., Yan, C., Heikkinen, L., Äijälä, M., Daellenbach, K. R., Zha, Q., Riva,
- 1112 M., Garmash, O., Junninen, H., Paatero, P., Worsnop, D., and Ehn, M.: Insights into atmospheric
- oxidation processes by performing factor analyses on subranges of mass spectra, Atmospheric Chem.
- Phys., 20, 5945–5961, https://doi.org/10.5194/acp-20-5945-2020, 2020.
- Zhao, D., Pullinen, I., Fuchs, H., Schrade, S., Wu, R., Acir, I.-H., Tillmann, R., Rohrer, F., Wildt,
- 1116 J., Guo, Y., Kiendler-Scharr, A., Wahner, A., Kang, S., Vereecken, L., and Mentel, T. F.: Highly
- 1117 oxygenated organic molecule (HOM) formation in the isoprene oxidation by NO3 radical,
- 1118 Atmospheric Chem. Phys., 21, 9681–9704, https://doi.org/10.5194/acp-21-9681-2021, 2021.
- Il Zheng, P., Chen, Y., Wang, Z., Liu, Y., Pu, W., Yu, C., Xia, M., Xu, Y., Guo, J., Guo, Y., Tian, L.,
- 1120 Qiao, X., Huang, D. D., Yan, C., Nie, W., Worsnop, D. R., Lee, S., and Wang, T.: Molecular
- 1121 Characterization of Oxygenated Organic Molecules and Their Dominating Roles in Particle Growth
- in Hong Kong, Environ. Sci. Technol., 57, 7764–7776, https://doi.org/10.1021/acs.est.2c09252,
- 1123 2023.
- Ziemann, P. J. and Atkinson, R.: Kinetics, products, and mechanisms of secondary organic aerosol
- formation, Chem. Soc. Rev., 41, 6582, https://doi.org/10.1039/c2cs35122f, 2012.